Spectral properties and observables in ultracold Fermi gases

Eugen Dizer [,1] Jan Horak,[1] and Jan M. Pawlowski [1,2]

[1]*Institut für Theoretische Physik, Universität Heidelberg, Philosophenweg 16, 69120 Heidelberg, Germany*
[2]*ExtreMe Matter Institute EMMI, GSI, Planckstraße 1, 64291 Darmstadt, Germany*

We calculate nonperturbative self-consistent fermionic and bosonic spectral functions of ultracold Fermi gases with the spectral functional approach. This approach allows for a direct real-time computation of nonperturbative correlation functions, and in the present work we use spectral Dyson-Schwinger equations. We focus on the normal phase of the spin-balanced Fermi gas and provide numerical results for the full fermionic and bosonic spectral functions. The spectral functions are then used for the determination of the equation of state, the Tan contact, and ejection rf spectra at unitarity. These results are compared to experimental data, the self-consistent T-matrix approach, and lattice results. Our approach offers a wide range of applications, including the *ab initio* calculation of transport and spectral properties of the superfluid phase in the BCS-BEC crossover.

I. INTRODUCTION

Ultracold Fermi gases [1–3] represent a versatile tool for studying strongly correlated quantum systems at low energies. The experimental control over the system parameters allows for the investigation of a wide range of phenomena, such as the BCS-BEC crossover [4–8], the formation of polarons [9–13], and the emergence of superfluidity [14–16].

Strong correlations, e.g., close to unitarity [1], render the theoretical description of interacting Fermi gases a nonperturbative problem. Therefore, various nonperturbative approaches, such as quantum Monte Carlo (QMC) simulations [17,18], self-consistent T-matrix theory [19–22], and Dyson-Schwinger equation (DSE) [23–25] and functional renormalization group (fRG) [26–28] approaches, have been employed to describe the system. Various important properties of the gas, such as transport and scattering properties [29–31] and the excitation spectrum [32–34], are encoded in its spectral functions, which requires the computation of the fermionic and bosonic self-energies at real frequencies.

While QMC simulations are formulated at imaginary frequencies by construction, also functional methods such as the DSE and fRG approaches are usually formulated in Euclidean space-time due to significantly reduced computational costs. Then the computation of spectral functions requires an analytic continuation from Matsubara to real frequencies. While this is an ill-conditioned numerical task accompanied by large systematic uncertainties [35] (see also [36,37] for further discussions and developments), the advantage lies in its simple use and fast generation of new imaginary-time results. Respective results can be found, e.g., in [38,39].

Due to the large systematic uncertainties, direct real-time computations are much preferable and have been performed in similar quantum systems, e.g., in [40–48]. Most of these works use a self-consistent T-matrix approximation and the integrals are computed by employing various numerical techniques.

Recently, the *spectral functional approach* was put forward in [49], which utilizes directly the spectral representation of propagators and vertices: Inserting them into nonperturbative diagrams in a given functional approach, the respective frequency sums or integrals can be performed analytically, and the remaining real spectral integrals are readily computed numerically. This allows for a direct computation of the spectral functions in terms of spectral loop integrals. The spectral functional approach has been developed within the framework of Dyson-Schwinger equations, but it applies to all functional approaches. The spectral functional renormalization has been set up and used in [50,51], and the spectral approach is tailor-made for application in two-particle irreducible (2PI) resummation schemes [52], where all correlation functions are constructed from nonperturbative propagators. It has been successfully used for the nonperturbative computation of spectral functions and bound-state properties in scalar theories [49,53,54], gauge theories [55–58], and quantum gravity [50].

In this work we use the spectral functional approach for the computation of nonperturbative self-consistent single-particle spectral functions in the normal phase of a strongly interacting spin-balanced Fermi gas for all scattering lengths a and in particular close to a Feshbach resonance [59] with $a \to \infty$. This constitutes an application of the spectral functional approach [49] to nonrelativistic systems. Specifically, we set up spectral Dyson-Schwinger equations for the fermionic and bosonic self-energies at real frequencies, yielding direct access to their spectral functions. Notably, our approach allows for the simultaneous calculation of the fermionic single-particle and the bosonic two-particle (dimer) spectral function at no additional cost. With the spectral functions we also determine the density equation of state [16], the Tan contact [60], and ejection rf spectra [7] at unitarity. Our results agree with results from the self-consistent T-matrix approximation [19,38], but the flexibility of the spectral functional approaches gives access to more generic expansion schemes.

The present paper is organized as follows. In Sec. II we introduce our microscopic model for the spin-balanced Fermi gas. In Sec. III we set up the spectral Dyson-Schwinger

equations for bosonic and fermionic propagators. Our numerical results for the spectral functions as well as the density, rf spectra, and Tan contact are presented in Sec. IV. We summarize and provide an outlook for future work in Sec. V.

II. MICROSCOPIC MODEL

We consider a nonrelativistic two-component Fermi gas described by the Euclidean classical action

$$S[\psi] = \int_0^\beta d\tau \int d^3x \left(\sum_{\sigma=\uparrow,\downarrow} \psi_\sigma^*(\partial_\tau - \nabla^2 - \mu_\sigma)\psi_\sigma \right.$$
$$\left. + \lambda \psi_\uparrow^* \psi_\downarrow^* \psi_\downarrow \psi_\uparrow \right), \tag{1}$$

where λ is the coupling constant of the contact interaction. If used on the mean-field level, λ would be related directly to the scattering length a via [28]

$$\lambda = 8\pi a. \tag{2}$$

Instead of using the common split into bare coupling and cutoff contribution, Eq. (2) is readily converted into a cutoff-independent relation including quantum effects [for more details see Sec. III and Appendix A, in particular (A1) and (A2)].

In (1) we also introduced the chemical potential of the fermion species, μ_σ with $\sigma = (\uparrow, \downarrow)$. The fermionic fields $\psi_\sigma(\tau, \mathbf{x})$ are Grassmann valued and depend on the Euclidean time τ, which is restricted to the circumference $\beta = 1/T$, and the spatial coordinates $\mathbf{x}$. In (1) we also used natural units $\hbar = k_B = 2m_\psi = 1$, where m_ψ is the mass of fermions.

The emergence of bosonic dimers and their condensation at low temperatures in the fermionic ultracold gas can be efficiently accommodated by rewriting the action (1) with a Hubbard-Stratonovich transformation. Thus, we will consider a spin-balanced system ($\mu_\uparrow = \mu_\downarrow = \mu$), where the contact interaction of fermions with opposite spin is replaced by the exchange of bosonic dimers,

$$S[\psi, \phi] = \int_0^\beta d\tau \int d^3x \left(\sum_{\sigma=\uparrow,\downarrow} \psi_\sigma^*(\partial_\tau - \nabla^2 - \mu)\psi_\sigma \right.$$
$$\left. + \nu\phi^*\phi - h(\phi^*\psi_\uparrow\psi_\downarrow - \phi\psi_\uparrow^*\psi_\downarrow^*) \right), \tag{3}$$

where h is the Feshbach coupling between the fermions and bosons and ν is the detuning of the dimer. On the mean-field level, similarly to (2), the couplings and the detuning parameter would be related by

$$\lambda = -\frac{h^2}{\nu}. \tag{4}$$

For the full relation on the quantum level, see Sec. III and Appendix A, in particular (A1) and (A2).

It is readily shown that (3) reduces to (1) in the equation of motion (EOM) of ϕ, also using (4). Solving (4) for the detuning parameter on the full quantum level leads to (A2) in Appendix A. Notably, while the four-fermion coupling λ gets strongly affected by fluctuations, the Feshbach coupling h is

well approximated by its classical value, as these fluctuation effects are encoded in ν. The latter is used to tune the (inverse) scattering length (for a detailed discussion of all these properties see [28]). We also emphasize that the absence of an explicit s-channel four-fermion scattering can be sustained on the quantum level within the fRG approach with emergent composites or rebosonization (for the respective conceptual developments see [61–64] and for an application to the present system see [65,66]). Heuristically, this approach may be understood as a scale-dependent Hubbard-Stratonovich transformation.

For a dilute ultracold Fermi gas, the effective range r_0 of the interaction is of the order of the inverse van der Waals length l_{vdW} and defines a physical momentum cutoff scale $\Lambda \sim 1/r_0$, which is much larger than all relevant physical scales ($\Lambda \gg k_F$). Throughout this work we work in the limit of contact interactions with zero effective range such that Λ can be sent to infinity in the end. For a more detailed discussion of the renormalization scheme, refer to Appendix A.

The complex bosonic field $\phi(\tau, \mathbf{x})$ was introduced as an efficient book-keeping device for the s-channel interaction between fermions of opposite spin. For example, bubble resummations of s-channel diagrams but also beyond bubble resummations of t and u-channel contributions are encoded in two-point function diagrams or corrections to the Yukawa coupling. More importantly, emergent dynamical s-channel dimer degrees of freedom are already taken care of as is their condensation.

Hence, by tuning the dimensionless interaction strength $(k_F a)^{-1}$, the system can be driven from a BCS-type superfluid to a Bose-Einstein condensed state, allowing for the exploration of the BCS-BEC crossover [44,67–69]. Here the interaction strength is measured in terms of the Fermi momentum

$$k_F = (3\pi^2 n)^{1/3}, \quad T_F = \varepsilon_F = k_F^2, \tag{5}$$

where n is the total density and we have also defined the Fermi energy and temperature for later use. On the BCS side of the crossover $(k_F a)^{-1} < 0$, the bosonic dimer ϕ describes weakly bound Cooper pairs. On the BEC side $(k_F a)^{-1} > 0$, ϕ describes tightly bound bosonic molecules. Bose-Einstein condensation of the bosonic pairs, i.e., a nonvanishing expectation value of ϕ, leads to superfluidity in the system. In the following we consider the normal phase of the BCS-BEC crossover with a special focus on the strongly correlated unitary regime at $(k_F a)^{-1} = 0$.

III. SPECTRAL DYSON-SCHWINGER EQUATIONS

In this section we briefly introduce the coupled spectral propagator DSEs which will be used in obtaining all numerical and analytical results in this work. We also specify the underlying approximation of the effective action.

A. Gap equations and the approximation of the effective action

Functional approaches, such as the DSEs and the fRG or 2PI resummation schemes, provide exact nonperturbative relations for correlation functions in terms of full propagators and vertices (fRG) as well as the classical vertices (DSE
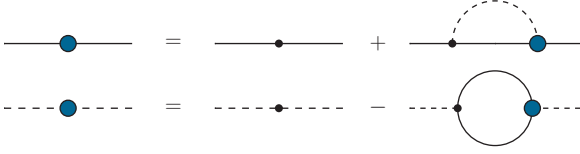
FIG. 1. Fermion (solid line) and boson (dotted line) propagator Dyson-Schwinger equation for balanced ultracold Fermi gases in the normal phase. The notation is as defined in Fig. 2

and 2PI). For reviews, see [70] (DSEs) and [71–75] (fRG) and [52] (2PI). The central object in these approaches is the quantum effective action $\Gamma[\Phi]$, which is the generating functional of 1PI correlation functions, or the 2PI effective action. Correlation functions of n fields are obtained by n functional derivatives with respect to the mean fields, $\Phi = (\psi_\sigma, \psi_\sigma^*, \phi, \phi^*)$, where for the sake of notational simplicity we have used the same expressions as for the classical fields.

The most important example is the full nonperturbative two-point function, the full propagator G_Φ, which is the pivotal building block of all diagrammatic functional approaches. In terms of the 1PI effective action, it is given as the inverse of the 1PI two-point function $G_\Phi = [\Gamma^{(2)}]_{\Phi\Phi^*}^{-1}$, which is a matrix inverse in field space. In the normal phase, the expectation value of the bosonic field is zero, i.e., $\phi = 0$, and the propagator, if evaluated on the EOMs, is diagonal in field space. Since we are dealing with a balanced system, the propagators of the $\uparrow$ and $\downarrow$ species are the same and we are left with only one fermion propagator $G_{\psi_\uparrow} = G_{\psi_\downarrow} = G_\psi$ and one boson propagator G_ϕ. The gap equation or DSE for the inverse propagator $\Gamma_{\Phi\Phi^*}^{(2)}$ involves the classical inverse propagator $S_{\Phi\Phi^*}^{(2)}$, whose fermionic and bosonic components are obtained from the microscopic action (3),

$$S_{\psi\psi^*}^{(2)}(P) = -i\omega_n + \boldsymbol{p}^2 - \mu, \quad S_{\phi\phi^*}^{(2)}(Q) = \nu. \quad (6)$$

Here $P = (\omega_n, \boldsymbol{p})$ and $Q = (\epsilon_n, \boldsymbol{q})$ with the fermionic (ω_n) and bosonic (ϵ_n) Matsubara frequencies, respectively,

$$\omega_n = (2n+1)\pi T, \quad \epsilon_n = 2n\pi T. \quad (7)$$

The coupled Dyson-Schwinger equations for the fermion and boson propagator are depicted in Fig. 1, while the diagrammatic notation is summarized in Fig. 2. The renormalized fermion and boson gap equations are given by

$$G_\psi^{-1}(P) = -i\omega_n + \boldsymbol{p}^2 - \mu + \Sigma_\psi(P),$$
$$G_\phi^{-1}(Q) = -\frac{h^2}{8\pi a} - \Pi_\phi(Q), \quad (8)$$

with the renormalized fermionic and bosonic self-energies $\Sigma_\psi(P)$ and $\Pi_\phi(Q)$, respectively. For more details on the spectral renormalization procedure see Appendix A.

FIG. 2. Diagrammatic notation used throughout this work. Lines stand for full propagators, small dots stand for classical vertices, and larger dots stand for full vertices.

Now we specify the approximation of the effective action used for the following computations. As already discussed below (4), the approximation of a classical constant Yukawa coupling h is working well as the fluctuations of the four-fermion interaction are well captured by that in the detuning parameter. The latter is part of the full propagator and hence will be accessed here. This approximation is readily lifted by also solving the spectral DSE for the Yukawa coupling and the remnant four-fermion interaction, which will be considered elsewhere. This leads us to the approximation of the renormalized finite effective action

$$\Gamma[\psi, \phi] = \int_0^\beta d\tau \int d^3x[\psi_\sigma^*(\partial_\tau - \nabla^2 - \mu + \Sigma_\psi)\psi_\sigma$$
$$+ \phi^*(\nu - \Pi_\phi)\phi - h(\phi^*\psi_\uparrow\psi_\downarrow - \phi\psi_\uparrow^*\psi_\downarrow^*)], \quad (9)$$

where the spin sum over $\sigma = \uparrow, \downarrow$ is implied. Equation (9) includes the full frequency- and momentum-dependent fermionic and bosonic propagator and keeps the classical interaction part. This approximation incorporates the s-channel bubble resummation with full fermionic propagators in Σ_ψ as the bosonic dimer propagator simply constitutes the bubble chain.

Using (3) and (9) on both sides of the gap equations (8) leads us to the diagrammatic expression for the nonperturbative self-consistent and renormalized self-energies at finite temperature,

$$\Pi_\phi(Q) = h^2 \int_{\boldsymbol{p}} \left(T \sum_{\omega_m} G_\psi(P)G_\psi(Q-P) - \frac{1}{2\boldsymbol{p}^2} \right),$$
$$\Sigma_\psi(P) = h^2 \int_{\boldsymbol{q}} T \sum_{\epsilon_m} G_\phi(Q)G_\psi(Q-P), \quad (10)$$

with

$$\int_{\boldsymbol{q}} = \int \frac{d^3q}{(2\pi)^3}, \quad (11)$$

and similarly for the integral over $\boldsymbol{p}$. The subtraction with $-1/2\boldsymbol{p}^2$ on the right-hand side of the equation for Π_ϕ in (10) arises from the spectral renormalization. Equation (10) is given by Fig. 1 with two classical vertices in each diagram. Note also that in the fermionic self-energy $\Sigma_\psi(P)$, the sum is over bosonic Matsubara frequencies $\epsilon_m = 2m\pi T$, whereas in the bosonic self-energy $\Pi_\phi(Q)$, the sum is over fermionic Matsubara frequencies $\omega_m = (2m+1)\pi T$.

Evidently, the present truncation with $\Gamma^{(3)} = S^{(3)}$ in the gap equations, i.e., (10) derived from (9), is equivalent to an s-channel bubble resummation, also known as the self-consistent T-matrix approximation [22,38,76]. It has been argued in the literature that the inclusion of self-consistency without the simultaneous inclusion of vertex corrections may lead to incorrect results for dynamical quantities, e.g., the violation of the conservation laws for energy and further conserved quantities can lead to secular behavior in a nonequilibrium evolution. We note that the present functional approach can be generalized straightforwardly by taking the full three-point function $\Gamma^{(3)}$ into account, as has been done in [49,53] for a scalar theory. However, this topic requires a

dedicated study, which goes beyond the scope of the present work.

B. Spectral representation

The spectral representation of the propagator is at the core of the spectral functional approach developed in [49]. In the present work we employ the Källén-Lehmann representation of the full propagators [38,77,78]

$$G(\omega_n, \boldsymbol{p}) = \int_{-\infty}^{\infty} d\lambda \frac{\rho(\lambda, \boldsymbol{p})}{-i\omega_n + \lambda}, \tag{12}$$

where $\rho(\lambda, \boldsymbol{p})$ is the frequency- and momentum-dependent spectral function. In this way, the spectral function acts as a linear response function of the propagator, encoding the energy spectrum of the theory. Equation (12) leads to the inverse relation between the spectral function and the retarded propagator

$$\rho(\omega, \boldsymbol{p}) = \frac{1}{\pi} \text{Im} G^R(\omega, \boldsymbol{p}), \tag{13}$$

where $G^R(\omega, \boldsymbol{p}) = G(-i(\omega + i0^+), \boldsymbol{p})$ and ω is now a real frequency. Note that (13) always defines the spectral function, related to the statistical function by the fluctuation-dissipation theorem, whereas (12) only holds true for fields that define physical asymptotic states. While this is true in the present ultracold gas, it is far from obvious for theories defined in terms of unphysical degrees of freedom such as gauge fields (for more details see [55–57]). In summary, the present ultracold gas is optimally suited for application of spectral functional approaches.

The existence of a spectral representation restricts all non-analyticities of the propagator to lie on the real frequency and momentum axis. The fermion spectral function satisfies the sum rule

$$\int_{-\infty}^{\infty} d\lambda \, \rho_\psi(\lambda, \boldsymbol{p}) = 1. \tag{14}$$

The fermionic spectral functions satisfy $\rho_\psi(\omega, \boldsymbol{p}) \geqslant 0$. In our approach, the frequency and momentum dependence of the bosonic inverse propagator is only given by the self-energy [see Eq. (8)]. Accordingly, its spectral function is not that of a physical state and is not normalized to unity like the fermionic one. Moreover, the respective spectral function is not positive semidefinite but satisfies $\text{sgn}(\omega)\rho_\phi(\omega, \boldsymbol{p}) \geqslant 0$ [78]. Note that the negative sign of the boson spectral function for negative frequencies guarantees the positivity of the bosonic momentum distribution function [47].

Using the spectral representation (12) for the fermion and boson propagator, the self-energies can be written in terms of spectral loop integrals. We find for the bosonic self-energy

$$\Pi_\phi(\epsilon_n, \boldsymbol{q}) = h^2 \int_{\boldsymbol{p}} \left(\int_{\lambda_1, \lambda_2} \rho_\psi(\lambda_1, \boldsymbol{p}) \rho_\psi(\lambda_2, \boldsymbol{q} - \boldsymbol{p}) \right.$$

$$\left. \times T \sum_{\omega_m} \frac{1}{i\omega_m - \lambda_1} \frac{1}{i(\epsilon_n - \omega_m) - \lambda_2} - \frac{1}{2\boldsymbol{p}^2} \right). \tag{15}$$

The fermionic self-energy takes the form

$$\Sigma_\psi(\omega_n, \boldsymbol{p}) = h^2 \int_{\lambda_1, \lambda_2, \boldsymbol{q}} \rho_\phi(\lambda_1, \boldsymbol{q}) \rho_\psi(\lambda_2, \boldsymbol{q} - \boldsymbol{p})$$

$$\times T \sum_{\epsilon_m} \frac{1}{i\epsilon_m - \lambda_1} \frac{1}{i(\epsilon_m - \omega_n) - \lambda_2}. \tag{16}$$

In both (15) and (16) we have used (11) and

$$\int_\lambda = \int_{-\infty}^{\infty} d\lambda. \tag{17}$$

Importantly, the Matsubara sum in (16) and (15) can be carried out analytically. This leaves us with symbolic expressions in terms of the argument ϵ_n and ω_n for both self-energies that can be evaluated at any complex frequency. The explicit spectral integral expressions for Σ_ψ and Π_ϕ can be found in Appendixes B and C.

We close this section with a brief discussion of the existence of a spectral representation and its relation to the self-consistent solution of the gap equations above. Here *self-consistent* refers to the use of the same spectral function on both sides of the gap equation, hence providing a solution of the gap equation: If the iterative solution of the self-consistent coupled set of spectral gap equations, described in Appendix E, converges, it entails already the existence of the spectral representation for fermionic atoms and dimers in the given approximation. This is discussed further in Appendix D, where we also provide additional numerical evidence by comparing the spectral representation to the diagrammatic results at imaginary frequencies for both fermion and dimer propagators. A direct consequence of this self-consistent solution of the gap equations is the existence of a spectral representation for the bosonic dimer in the current approximation (a related discussion can be also found in [42,44,46]). Let us emphasize that the notion of self-consistency in the T-matrix approach refers to a diagrammatic self-consistency. Note that in general these two notions do not agree, but they agree within the approximation used in the present work.

C. Evaluation at real frequencies

The regularized and coupled DSEs in Eq. (8) can be evaluated for arbitrary complex frequencies. For the extraction of the spectral functions with (13), we choose $\omega_n = -i(\omega + i\varepsilon)$ with $\varepsilon \to 0^+$. The limit $\varepsilon \to 0^+$ is performed analytically using the relation

$$\frac{1}{x \pm i0^+} = P\left(\frac{1}{x}\right) \mp i\pi\delta(x), \tag{18}$$

where $P(1/x)$ denotes the principal value of $1/x$. This allows us to write the imaginary part of the retarded self-energies as

$$\text{Im}\Pi_\phi^R(\omega, \boldsymbol{q}) = \pi h^2 \int_{\lambda, \boldsymbol{p}} \rho_\psi(\omega - \lambda, \boldsymbol{p}) \rho_\psi(\lambda, \boldsymbol{q} - \boldsymbol{p})$$

$$\times [1 - n_F(\omega - \lambda) - n_F(\lambda)], \tag{19}$$

$$\text{Im}\Sigma_\psi^R(\omega, \boldsymbol{p}) = \pi h^2 \int_{\lambda, \boldsymbol{q}} \rho_\phi(\omega + \lambda, \boldsymbol{q}) \rho_\psi(\lambda, \boldsymbol{q} - \boldsymbol{p})$$

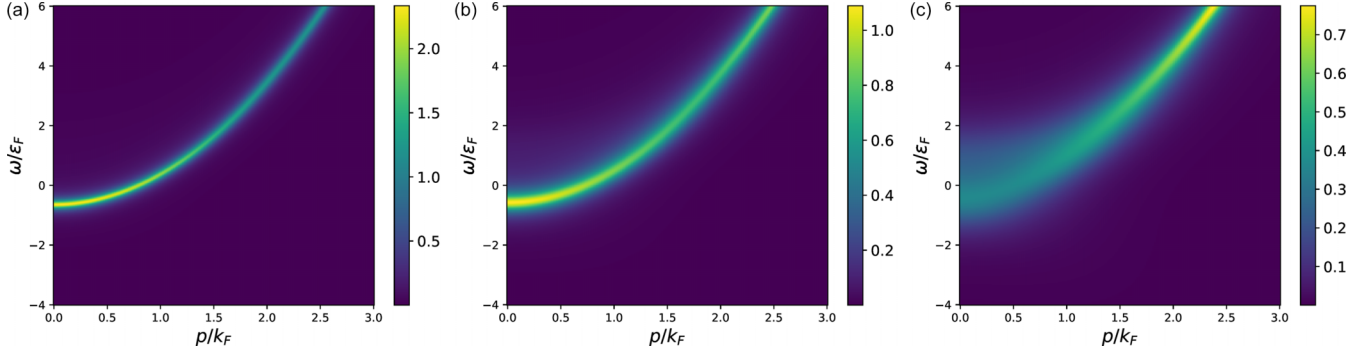$$\times [-n_B(\omega + \lambda) - n_F(\lambda)]. \tag{20}$$

FIG. 3. Results for the fermionic spectral function $\rho_\psi(\omega, \boldsymbol{p})\varepsilon_F$ for $T/T_F = 0.56$ at different interaction strengths (a) $(k_F a)^{-1} = -0.5$, BCS regime, $\beta\mu = 0.5$; (b) $(k_F a)^{-1} = 0$, unitarity, $\beta\mu = 0.13$; and (c) $(k_F a)^{-1} = 0.5$, BEC regime, $\beta\mu = -0.54$. Respective results for the imaginary-time propagator $G_\psi(\omega_n, \boldsymbol{0})\varepsilon_F$ at the same interaction strengths are shown in Fig. 13.

Here we have introduced the Fermi-Dirac distribution n_F and Bose-Einstein distribution n_B with

$$n_F(x) = \frac{1}{e^{x/T} + 1}, \quad n_B(x) = \frac{1}{e^{x/T} - 1}. \tag{21}$$

Detailed derivations of the above formulas are deferred to Appendixes B and C. Note that the pole of $n_B(\omega + \lambda)$ in the fermion self-energy is exactly canceled by the zero crossing of the boson spectral function ρ_ϕ (see Sec. III B).

From the imaginary part of the fermion self-energy, e.g., the real part can be obtained via the Kramers-Kronig relation

$$\mathrm{Re}\,\Sigma_\psi^R(\omega, \boldsymbol{p}) = \frac{1}{\pi} P \int_\lambda \frac{\mathrm{Im}\,\Sigma_\psi^R(\lambda, \boldsymbol{p})}{\lambda - \omega}. \tag{22}$$

For the real part of the boson self-energy, the renormalization of ν has to be taken into account. The problematic vacuum part can be treated analytically (see Appendix E). This set of equations allows for an iterative calculation of the retarded self-energies and therefore a direct determination of the spectral functions which are presented in the next section. For a detailed discussion of the numerical implementation see Appendix E.

IV. RESULTS

In this section we discuss the numerical results for the fully-self-consistent spectral functions as well as their use for the computation of the density equation of state, the Tan contact, and ejection rf spectra at unitarity. In Sec. IV A we focus on the results obtained in real frequencies. In Sec. IV B we use the spectral functions from Sec. IV A to compute rf spectra in comparison to experimental data. Finally, in Sec. IV C we compute the equation of state and use the high-momentum dependence of the density to extract the Tan contact.

A. Spectral functions

We present numerical results for the self-consistent spectral functions of the spin-balanced Fermi gas in the normal phase at different scattering lengths and in particular at unitarity. Physical properties of the single-particle fermion spectral function have been discussed extensively in the literature [33,38,79]. In this work we also discuss the bosonic two-particle (dimer) spectral function, which has not received

much attention in the past. For details on the numerical implementation, we refer the reader to Appendix E.

Figure 3 shows results for the full frequency- and momentum-dependent fermion spectral function ρ_ψ and Fig. 4 shows the corresponding bosonic dimer spectral functions ρ_ϕ for different interaction strengths $1/k_F a$, with the Fermi momentum k_F defined in (5). Furthermore, Fig. 5 shows results for the fermionic spectral function ρ_ψ at $\boldsymbol{p} = 0$ for the unitary Fermi gas at different temperatures, which are used for the computation of the rf spectra in Sec. IV B. In Figs. 3–5 the frequency ω and momentum $\boldsymbol{p}$ are measured in the Fermi energy ε_F and k_F, respectively, and the fermionic (bosonic) spectral functions have units of ε_F^{-1} ($\varepsilon_F^{-1/2}$). We state all results in dimensionless form. Note that the bosonic dimer spectral function is not normalized and depends on the choice of the Feshbach coupling h. This is connected to it being a pure interaction exchange boson and not a real particle. To eliminate the h dependence, we multiply ρ_ϕ by $h^2/8\pi$ since $h^2 G_\phi/8\pi$ is the relevant quantity, which is related to the scattering amplitude (see Appendix A).

Our results are computed directly in real time and agree qualitatively with the reconstruction results from previous works for the fermion spectral function [38]. It is well known that numerical reconstruction problems are ill-conditioned or at least have a high condition number. Moreover, the respective ambiguities are specifically large in the low-frequency regime at finite temperature. The computation of dynamical properties such as the shear viscosity requires a precise determination of the low-frequency regime and its transport peaks, which can be achieved with our spectral functional approach. We envisage a two-step process with a direct use of Euclidean benchmark results for a quality check of the direct spectral computation as well as using its structural low-frequency properties as an inductive bias for spectral reconstructions. This allows for direct access to the spectral properties of ultracold gases while maintaining the quantitative thermodynamic results of imaginary-time approaches. In summary, this fully justifies the increased numerical costs.

The results for the bosonic dimer spectral function encode important information about the physics of the ultracold Fermi gas and are consistent with previous studies. First, we observe a very broad peak structure for weak attractive interactions in the BCS regime and a very sharp peak structure with thermal broadening for strong attractive interactions in the
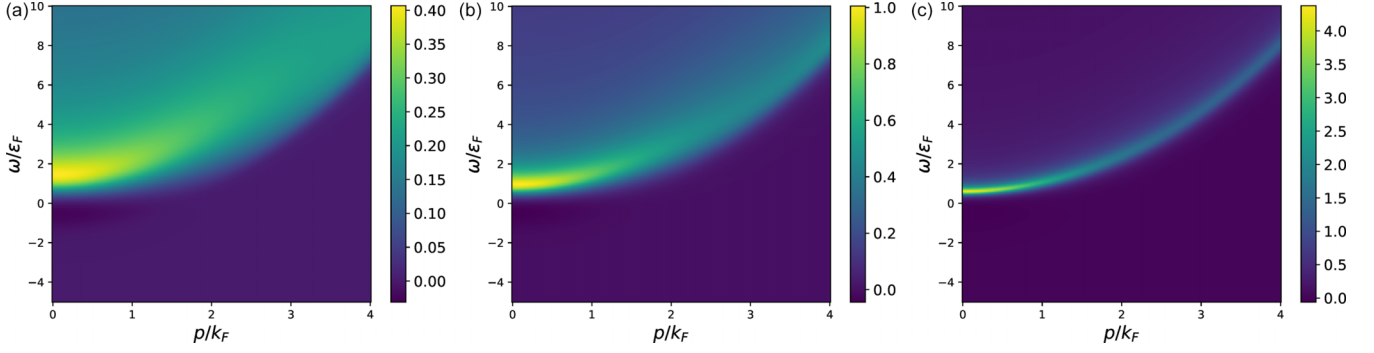
FIG. 4. Results for the bosonic dimer spectral function $h^2 \rho_\phi(\omega, \boldsymbol{p}) \sqrt{\varepsilon_F}/(8\pi)$ for $T/T_F = 0.56$ at different interaction strengths (a) $(k_F a)^{-1} = -0.5$, BCS regime, $\beta\mu = 0.5$; (b) $(k_F a)^{-1} = 0$, unitarity, $\beta\mu = 0.13$; and (c) $(k_F a)^{-1} = 0.5$, BEC regime, $\beta\mu = -0.54$. Respective results for the imaginary-time propagator $h^2 G_\phi(\varepsilon_n, \boldsymbol{0}) \sqrt{\varepsilon_F}$ at the same interaction strengths are shown in Fig. 14.

BEC regime. The latter property signals the tightly bound molecules on the BEC side. On this side of the BCS-BEC phase diagram at $1/k_F a = 0.5$, the boson spectral function is very sharp and the system can be described as a normal Bose liquid. On the BCS side of the crossover at $1/k_F a = -0.5$, the fermion spectral function is sharper and the system is described as a normal Fermi liquid.

Additionally, the boson spectral function reveals crucial information about the critical region of the phase transition to the superfluid state. The onset of superfluidity is marked by the divergence of the boson propagator at zero frequency and momentum $G_\phi^{-1}(0, \boldsymbol{0}) = 0$. This property is known as the Thouless criterion [80]. Thus, the closer and sharper the peak gets at zero frequency and momentum, the closer the system is to the phase transition, until the spectral function eventually diverges at the critical temperature. We refrain from a respective analysis and only present results in the normal phase.

Computations at and below the phase transition are beyond the scope of the present paper and will be considered elsewhere. Note, however, that respective work in the spectral functional approach has already been done in relativistic systems with both the DSE and the fRG [49,53,54]. The approximations there go beyond that used in the present work. In [49,53,54], the full s-channel resummation of the four-point

function was considered, as well as additional diagrams that arise in the presence of a condensate ϕ_0. In contrast to the Monte Carlo (MC) integration routine used here, we used efficient integration routines in [49,53,54], aiming at optimal convergence for low-dimensional integrals. The use of adaptive MC integrators in the present work has to be understood as a test case for higher-dimensional computations as will arise for nontrivial vertex approximations beyond mere sums of momentum channels. This may be relevant in the presence of competing order effects.

In summary, we emphasize that the present spectral functional approach allows for a very efficient numerical implementation. Indeed, one of the reasons for setting up the spectral functional approach was its numerical efficiency, which by now has been proven in abundance in [49,50,53–58]. These successful tests include its convergence in coupled sets of integral equations, as well as the evaluation of bound-state properties in the broken phase as well as through the phase transition from the symmetric to the broken phase. Specifically, self-consistent real-time computations in the broken phase have so far solely been done in the present approach and standard Bethe-Salpeter-type computations. We add that, given the structural similarities of the approaches used in [81], as well as [82], to the spectral functional approach, it should be possible to extend the former approaches towards the broken regime along the lines of [49,53,54].

B. Radio-frequency spectroscopy

Now we use our numerical results for the spectral functions to compute experimentally measurable rf spectra [83–85]. We compare the results from our approach, obtained for the spin-balanced Fermi gas at unitarity, with recent experimental data from [7]. Specifically, we apply the relation

$$I(\omega) = \int_{\boldsymbol{q}} \rho_\psi(\varepsilon_{\boldsymbol{q}} - \omega - \mu, \boldsymbol{q}) n_F(\varepsilon_{\boldsymbol{q}} - \omega - \mu) \qquad (23)$$

for the computation of rf spectra $I(\omega)$ from the fermion spectral functions ρ_ψ (see [83,86]). In Eq. (23), $\varepsilon_{\boldsymbol{q}} = \boldsymbol{q}^2$ is the classical fermion dispersion.

Note that the chemical potential $\mu(T)$ is temperature dependent and has to be determined self-consistently from the density equation (25) below (see also [19,87–90]). More explicitly, the number density $n = 1/3\pi^2$ is fixed by the choice
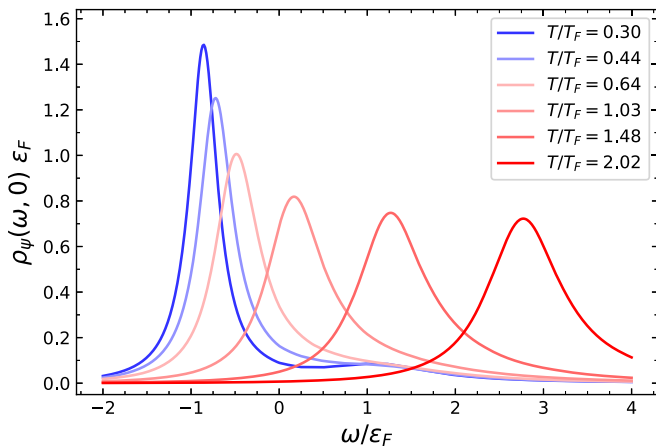

FIG. 5. Results for the fermionic spectral function $\rho_\psi(\omega, \boldsymbol{0})\varepsilon_F$ for the unitary Fermi gas at different temperatures, which are used for the computation of the rf spectra.
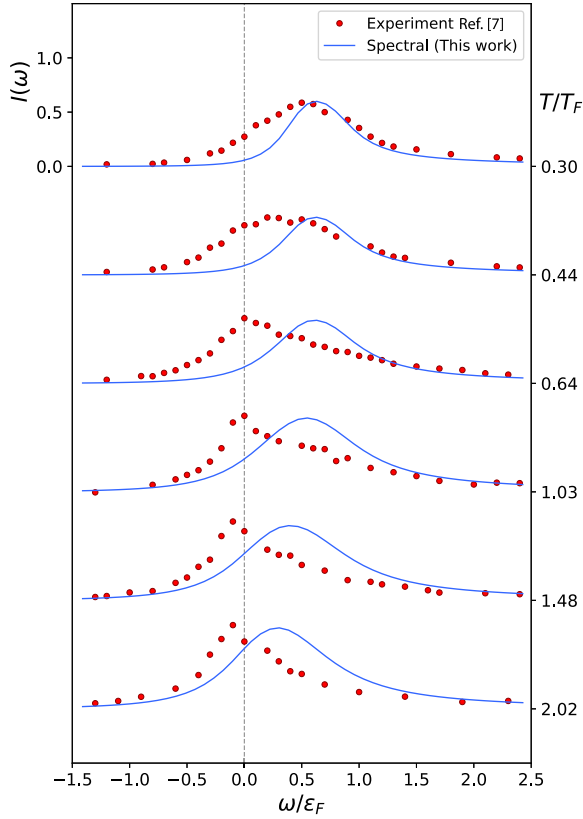
FIG. 6. Calculated ejection rf spectra $I(\omega)$ for the spin-balanced unitary Fermi gas as a function of the reduced temperature T/T_F. Results of this work (solid lines) are compared to experimental data from [7] (circles). A Fourier broadening of $0.1\varepsilon_F$ to account for the finite experimental resolution and a right shift by $0.09\varepsilon_F$ to account for the final-state interaction were applied.

$k_F = 1$, and temperature is measured in units of T_F. Consequently, the chemical potential $\mu(T)$ has to be chosen such that the density remains constant. One readily observes that the rf spectrum is normalized to the total density n [88],

$$n = 2 \int_\lambda I(\lambda). \tag{24}$$

Figure 6 shows our results in comparison with the experimental data from [7]. Apart from adjusting the peak heights, no fitting parameters have been used. In order to account for the finite rectangular rf pulse duration and thus a finite experimental resolution, a Fourier broadening of $0.1\varepsilon_F$ has been applied. Additionally, the curves have been right-shifted by an amount of $0.09\varepsilon_F$ to compensate for residual final-state interactions [48]. Even after taking into account all these possible factors, the calculated rf spectra do not fit the experimental data for higher temperatures very well. This is also apparent in the comparison of the peak position and full width as shown in Fig. 7.

This discrepancy was already observed in [48] for the case of a highly-spin-imbalanced unitary Fermi gas with the non-self-consistent T-matrix approach and persists in the very recent update in [91]. It was argued in [48] that the misalignment may be caused by the missing vertex corrections, which may also be relevant for pseudogap effects above T_c [92].
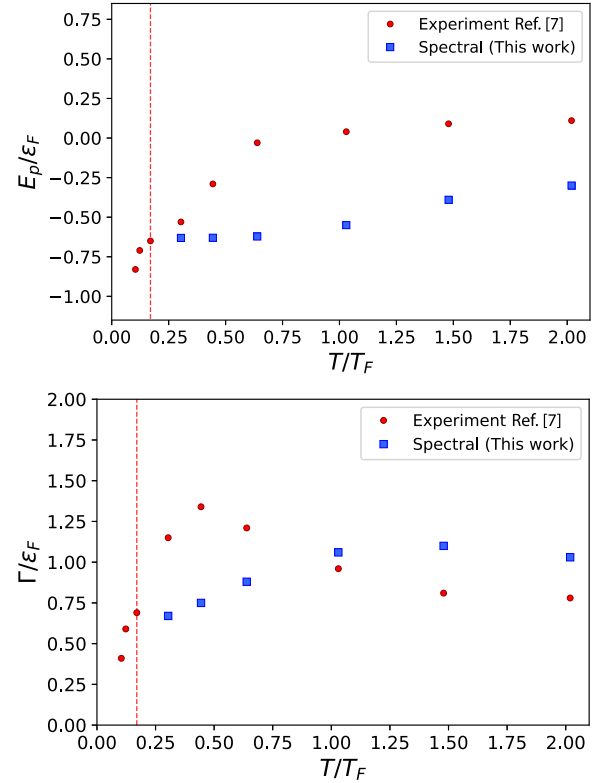

FIG. 7. Peak positions ($E_p = -\omega_p$) and full width at half maximum Γ as a function of the reduced temperature T/T_F. The vertical dashed line marks the transition to the superfluid phase.

Another possible explanation might be the absence of a trap average (see, e.g., [93]).

C. Equation of state and Tan contact

Finally, we use the present results for the spectral functions to compute the equation of state for the unitary Fermi gas. Thermodynamic quantities, such as the total particle density, can be calculated precisely in imaginary frequencies without the need of analytic continuation. For this reason, it is a good way to validate the new spectral approach against well-tested and robust imaginary-time calculations [19,94–99]. The total density n of fermions at finite chemical potential μ and temperature T can be calculated from the spectral function via [90]

$$n = 2 \int_{\boldsymbol{p}} T \sum_{\omega_n} G_\psi(\omega_n, \boldsymbol{p}) e^{i\omega_n 0^+} = 2 \int_{\boldsymbol{p}} n(\boldsymbol{p}), \tag{25}$$

where the factor 2 accounts for both fermion species and $n(\boldsymbol{p})$ is the momentum distribution function

$$n(\boldsymbol{p}) = \int_\lambda \rho_\psi(\lambda, \boldsymbol{p}) n_F(\lambda). \tag{26}$$

For recent precision computations with functional approaches in the full phase structure of ultracold gases, see [100]. The high-momentum tail of $n(\boldsymbol{p})$ is related to the Tan contact [101,102]

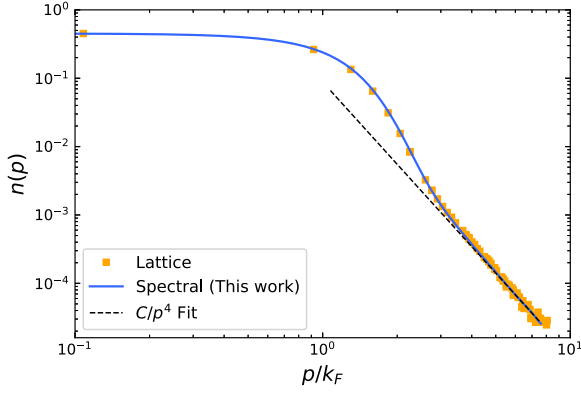$$\lim_{p \to \infty} n(\boldsymbol{p}) = \frac{C}{p^4}, \tag{27}$$

FIG. 8. Large-p behavior of the momentum density $n(p)$ of the balanced unitary Fermi gas at $T/T_F = 0.9$ ($\beta\mu = -0.5$). The $1/p^4$ tail for $p \gg k_F$ is clearly visible and the contact C can be determined from the fit. Lattice data are from [103]; see also [94].

where $p = \|\boldsymbol{p}\|$ and C is the contact parameter that can be determined from the fit. For a different computation in the DSE approach, see [25]. We have compared the present results for the momentum density $n(\boldsymbol{p})$ and the total density n with lattice data generated for this purpose with a Metropolis algorithm [103]. For results in the literature also see, e.g., [94,96,98], which use simulations with complex Langevin equations. The results for $n(\boldsymbol{p})$ in the present spectral DSE approach compare well to the benchmark results from the lattice simulation [103]. Moreover, in Fig. 8 we also show a fit to the high-momentum asymptotics and we deduce that the asymptotic $1/p^4$ tail is approached for

$$\|\boldsymbol{p}\| \gtrsim p_{\text{as}}, \quad p_{\text{as}} = 8k_F. \quad (28)$$

The Tan contact C is the slope of the asymptotics and, within the present approach, its value for $T/T_F = 0.9$ ($\beta\mu = -0.5$) is given by

$$C/k_F^4 \approx 0.084. \quad (29)$$

Equation (29) and further values for the Tan contact $C(\beta\mu)$ for other $\beta\mu$ are shown in Fig. 9 and will be used for the following
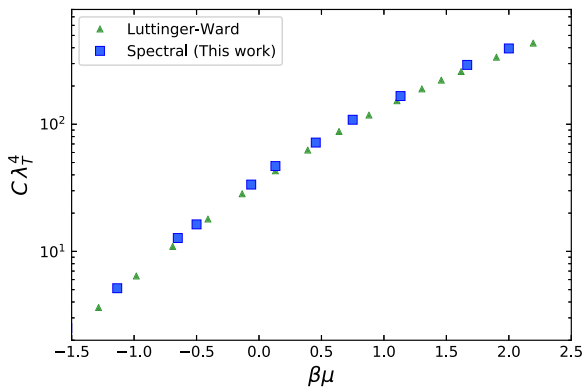

FIG. 9. Universal contact $C\lambda_T^4$, where $\lambda_T = \sqrt{4\pi\beta}$ is the thermal wavelength, of the spin-balanced unitary Fermi gas as a function of dimensionless chemical potential $\beta\mu$. Our results in real frequencies compare well with those of the Luttinger-Ward [19,95] and bold diagrammatic Monte Carlo [60] approaches.
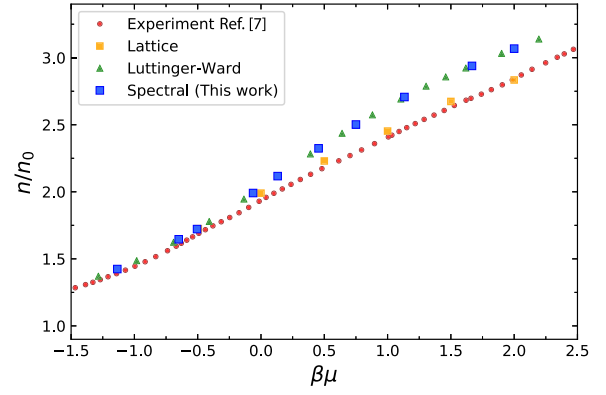

FIG. 10. Normalized density n/n_0 of the spin-balanced unitary Fermi gas as a function of dimensionless chemical potential $\beta\mu$. Results directly obtained in real frequencies (this work) are show in comparison with experimental data from Ref. [16], the lattice [103] (see also [96,98]), and the Luttinger-Ward approach [19,95].

determination of the density equation of state, which is an additional benchmark result: Figure 10 shows the results for the normalized density n/n_0 as a function of dimensionless chemical potential $\beta\mu$ in comparison with other approaches. The density n_0 of the noninteracting Fermi gas is given by

$$n_0 = 2\int_{\boldsymbol{p}} n_F(p^2 - \mu) = -2\,\text{Li}_{3/2}(-e^{\beta\mu})/\lambda_T^3, \quad (30)$$

where $\lambda_T = \sqrt{4\pi/T}$ is the thermal wavelength and $\text{Li}_{3/2}$ is a polylogarithmic function [104].

The computation of the total density (25) through the spectral function requires its high-momentum tail. For an efficient computation we split the momentum integral in (25) into parts with radial momenta smaller and larger than p_{as} defined in (28),

$$n = \sum_{\pm} \Delta n_{p_{\text{as}}}^{\pm}, \quad \Delta n_{p_{\text{as}}}^{\pm} = 2\int_{\|\boldsymbol{p}\| \gtrless p_{\text{as}}} n(\boldsymbol{p}). \quad (31)$$

The low-momentum part $\Delta n_{p_{\text{as}}}^{-}$ is computed directly from the spectral function, while we use the results for the asymptotic behavior of $n(\boldsymbol{p})$ for the high-momentum part $\Delta n_{p_{\text{as}}}^{+}$: Equation (27) provides us with an analytic form of the high-momentum distribution and we obtain

$$\Delta n_{p_{\text{as}}}^{+} = 2\int_{\|\boldsymbol{p}\| > p_{\text{as}}} \frac{C}{p^4} = \frac{C}{\pi^2 p_{\text{as}}}. \quad (32)$$

Here we have used $p_{\text{as}} = 10k_F$ in the explicit computation. Our real-time method reproduces the results of the well-tested Luttinger-Ward approach [19,95].

V. CONCLUSION

In the present work we have extended the spectral functional approach [49] for the nonperturbative and self-consistent computation of spectral properties in nonrelativistic systems. The approach was used for the direct real-time computation of fermionic single-particle and bosonic dimer spectral functions in the normal phase of a three-dimensional ultracold gas for a wide range of scattering lengths. The present results were benchmarked with observables in the

unitary limit of a spin-balanced Fermi gas: the equation of state, the Tan contact, and ejection rf spectra in comparison to other theoretical results and the experiment.

The present approach opens the path towards a wide range of applications, including transport properties and the *ab initio* calculation of spectral functions in the superfluid phase of ultracold Fermi gases [34,46,105], and through the phase transition, including the evaluation of critical properties of the system. Its potential for computations in the broken phase of quantum systems as well as in the critical regime has already been demonstrated in relativistic systems and the respective computational advances can directly be applied here. Furthermore, the present approach can also be readily applied to general spin and mass imbalance to study polaron physics or Fermi-Bose mixtures [106–108], where even the bosonic dimer spectral function can be measured using molecular injection spectroscopy [109]. Finally, we envisage the inclusion of vertex corrections or other classes of diagrams in systematic extensions towards full quantitative precision.

Note added. Recently, two works with complementary approaches for real-time computations on the Keldysh contour were published [81,82]. The respective results compare well with our results, and in combination this provides a systematic error control in particular within improvements. Furthermore, another independent work on the computation of self-consistent spectral functions of Fermi polarons was put forth very recently [91].

ACKNOWLEDGMENTS

APPENDIX A: RENORMALIZATION

The four-fermion model with the action (1) or equivalently its bosonized version with the action (3) requires regularization and renormalization. While either version of the present model has a physical cutoff given by the van der Waals length [see also the discussion below (4)], the respective standard renormalization procedure is accommodated in the present nonperturbative spectral approach with spectral renormalization (see [49,51]).

In the present approximation the renormalization procedure is easily implemented, following the standard renormalization procedure (see, e.g., [3,39,110]). To begin with, the physical renormalization condition can be extracted by the quantum analog of the classical relation between the two-body scattering length a in the vacuum and the full two-to-two scattering coupling at large distances λ. In the present

approximation this is simply the bubble-resummed four-fermion interaction and (2) turns into

$$-8\pi a = h^2 G_\phi(0, \mathbf{0}). \tag{A1}$$

This can be written in terms of the full physical detuning parameter

$$\nu = G_\phi^{-1}(0, \mathbf{0}) = \Gamma_{\phi\phi^*}^{(2)}(0, \mathbf{0}). \tag{A2}$$

Equation (A2) is the quantum analog of the classical relation (4) and constitutes a renormalization condition of the dimer gap equation. A renormalization at vanishing momentum and frequency in vacuum yields

$$\Pi_\phi(0, \mathbf{0}) = 0, \tag{A3}$$

which marks the detuning parameter in the effective action (9) as the physical one in (A2). The renormalization condition (A3) yields the renormalized boson DSE

$$G_\phi^{-1}(\epsilon_n, \mathbf{q}) = -\frac{h^2}{8\pi a}$$
$$- h^2 \int_{\mathbf{p}} \left(T \sum_{\omega_m} G_\psi(P) G_\psi(Q-P) - \frac{1}{2\mathbf{p}^2} \right). \tag{A4}$$

We have used the T independence of h in the present approximation together with the fact that the fermion propagator is classical in the present approximation (see [24,39]). In this approximation the renormalized vacuum result for $\Pi_\phi(Q)$ is readily obtained from (A4) by evaluating the self-energy loop integral with the classical fermion propagators

$$\Pi_\phi(\epsilon_n, \mathbf{p}) = h^2 \int_{\mathbf{q}} \left(\frac{1}{-i\epsilon_n + \varepsilon_{\mathbf{q}} + \varepsilon_{\mathbf{p}-\mathbf{q}}} - \frac{1}{2\varepsilon_{\mathbf{q}}} \right)$$
$$= -\frac{h^2}{8\pi} \sqrt{-\frac{i\epsilon_n}{2} + \frac{\mathbf{p}^2}{4}} \tag{A5}$$

for general complex frequencies $\epsilon_n \in \mathbb{C}$. This concludes our discussion of the renormalization of the bosonized theory within the present approximation.

APPENDIX B: BOSON SELF-ENERGY CALCULATION

In this Appendix we discuss the explicit computations and analytic results for the boson self-energy. Starting from (15), we define

$$\Pi_\phi(\epsilon_n, \mathbf{p}) = h^2 \int_{\mathbf{q}} \left(\int_{\lambda_1, \lambda_2} \rho_\psi(\lambda_1, \mathbf{q}) \rho_\psi(\lambda_2, \mathbf{p} - \mathbf{q}) \right.$$
$$\left. \times I(\epsilon_n, \lambda_1, \lambda_2) - \frac{1}{2\mathbf{q}^2} \right), \tag{B1}$$

with the analytic sum over fermionic Matsubara frequencies $\omega_m = (2m+1)\pi T$,

$$I(\epsilon_n, \lambda_1, \lambda_2) = T \sum_{\omega_m} \frac{1}{i\omega_m - \lambda_1} \frac{1}{i(\epsilon_n - \omega_m) - \lambda_2}$$
$$= \frac{1 - n_F(\lambda_1) - n_F(\lambda_2)}{-i\epsilon_n + \lambda_1 + \lambda_2}. \tag{B2}$$

Performing the analytic continuation $i\epsilon_n \to \omega + i0^+$ and taking the imaginary part, we end up with Eq. (19).

For the first iteration, analytic expressions for the self-energy at finite and zero temperature can be derived. Inserting the classical fermion spectral function $\rho_\psi(\lambda, \boldsymbol{p}) = \delta(\lambda - \boldsymbol{p}^2 + \mu)$, we obtain the well-known expression for the retarded boson self-energy [42,67,111]

$$\Pi_\phi^R(\omega, \boldsymbol{p}) = h^2 \int_q \left(\frac{1 - n_F(\varepsilon_q - \mu) - n_F(\varepsilon_{p-q} - \mu)}{-\omega + \varepsilon_q + \varepsilon_{p-q} - 2\mu - i0^+} - \frac{1}{2\varepsilon_q} \right), \tag{B3}$$

where $\varepsilon_p = \boldsymbol{p}^2$ is the classical momentum dispersion. The boson self-energy can be separated into a temperature-independent part and a temperature-dependent part,

$$\Pi_\phi^R = \Pi_\phi^{R,0} + \Pi_\phi^{R,T}. \tag{B4}$$

After the shift $\boldsymbol{q} \to \boldsymbol{q} + \boldsymbol{p}/2$, the angular integration is trivial, and we obtain the finite expression for the vacuum part

$$\Pi_\phi^{R,0}(\omega, \boldsymbol{p}) = \int_q \left(\frac{h^2}{-\omega + \varepsilon_q + \varepsilon_{p-q} - 2\mu - i0^+} - \frac{h^2}{2\varepsilon_q} \right)$$

$$= -\frac{h^2}{8\pi} \sqrt{-y - i0^+}, \tag{B5}$$

where we have defined $y = \omega/2 - p^2/4 + \mu$. The temperature-dependent part can be obtained analogously. We note that the contribution from both Fermi distributions is identical in the spin-balanced case and find

$$\Pi_\phi^{R,T}(\omega, \boldsymbol{p}) = -h^2 \int_q \frac{n_F(\varepsilon_q - \mu) + n_F(\varepsilon_{p-q} - \mu)}{-\omega + \varepsilon_q + \varepsilon_{p-q} - 2\mu - i0^+}$$

$$= -\frac{h^2}{4\pi^2} \int_0^\infty \frac{2\chi(q)q^2 dq}{q^2 - y - i0^+}, \tag{B6}$$

with the angle-integrated function

$$\chi(q) = \int_{-1}^1 \frac{dx}{2} n_F((\boldsymbol{q} \pm \boldsymbol{p}/2)^2 - \mu) = \begin{cases} n_F(q^2 - \mu) & \text{for} \quad p = 0 \\ \frac{T}{2pq} \ln\left(\frac{n_F(\mu - q_+^2)}{n_F(\mu - q_-^2)}\right) & \text{for} \quad p \neq 0, \end{cases} \tag{B7}$$

with $q_\pm = q \pm p/2$. Here $x = \cos(\theta_{pq})$ and θ_{pq} is the angle between the vectors $\boldsymbol{p}$ and $\boldsymbol{q}$. Note that this function yields a nonzero contribution in the vacuum for $\mu > 0$. In the limit $T \to 0$, the Fermi functions $n_F(x) \to \theta(-x)$ and the expression simplifies to

$$\chi^{T=0}(q) = \begin{cases} \theta(\mu - q^2) & \text{for} \quad p = 0 \\ \frac{\theta(\mu - q_-^2)}{2pq}[\mu - q_-^2 - (\mu - q_+^2)\theta(\mu - q_+^2)] & \text{for} \quad p \neq 0. \end{cases} \tag{B8}$$

The real and imaginary parts can be obtained analytically by using

$$\frac{1}{x - i0^+} = P\left(\frac{1}{x}\right) + i\pi\delta(x). \tag{B9}$$

There are the following two cases. If $y < 0$, the integrals for the real part are well defined and $\mathrm{Im}\,\Pi_\phi^{R,T} = 0$. If $y \geqslant 0$, the imaginary part is given analytically by

$$\mathrm{Im}\,\Pi_\phi^{R,T}(\omega, \boldsymbol{p}) = -\frac{h^2}{4\pi} \int_0^\infty dq\, 2\chi(q)q^2 \delta(q^2 - y) = -\frac{1}{4\pi}\sqrt{y}\,\chi(\sqrt{y}) \tag{B10}$$

and the real part $\mathrm{Re}\,\Pi_\phi^{R,T}$ can be obtained numerically via a one-dimensional principal value integral (see [48]).

For completeness, we also give the analytic expressions for the real part at $T = 0$. Since the contributions from both Fermi functions are identical, we obtain, for $\mathrm{Re}\,\Pi_\phi^{R,T=0}$ at zero temperature ($\mu > 0$),

$$\mathrm{Re}\,\Pi_\phi^{R,T=0}(\omega, \boldsymbol{p}) = \frac{h^2}{4\pi^2}\left[\sqrt{\mu} - \frac{y - \mu + \frac{p^2}{4}}{2p} \ln\left(\frac{y - \xi_+^2}{y - \xi_-^2}\right) - \sqrt{|y|} \times \begin{cases} \mathrm{arctanh}\left(\frac{\xi_-}{\sqrt{y}}\right) + \mathrm{arctanh}\left(\frac{\xi_+}{\sqrt{y}}\right) & \text{for } y \geqslant 0 \\ \arctan\left(\frac{\xi_-}{\sqrt{|y|}}\right) + \arctan\left(\frac{\xi_+}{\sqrt{|y|}}\right) & \text{for } y < 0 \end{cases} \right], \tag{B11}$$

with $\xi_\pm = \sqrt{\mu} \pm p/2$. The $p = 0$ limit is given by

$$\mathrm{Re}\,\Pi_\phi^{R,T=0}(\omega, \boldsymbol{0}) = \frac{h^2}{2\pi^2} \times \begin{cases} \sqrt{\mu} - \sqrt{y}\,\mathrm{arctanh}\left(\sqrt{\frac{\mu}{y}}\right) & \text{for } y \geqslant 0 \\ \sqrt{\mu} - \sqrt{|y|}\,\arctan\left(\sqrt{\frac{\mu}{|y|}}\right) & \text{for } y < 0. \end{cases} \tag{B12}$$

The contribution from the next iterations has to be computed numerically and gives rise to a finite correction on top of the analytic result. For more details on the numerical treatment see Appendix E. Finally, an exemplary plot of the fully converged boson self-energy $\Pi_\phi^R(\omega, \boldsymbol{p})$ is shown in Fig. 11.

APPENDIX C: FERMION SELF-ENERGY CALCULATION

For the fermion self-energy, the Matsubara sum can also be calculated analytically. However, there is no analytic result for the first iteration since the classical boson spectral function is not defined. Therefore, the fermion self-energy has to be
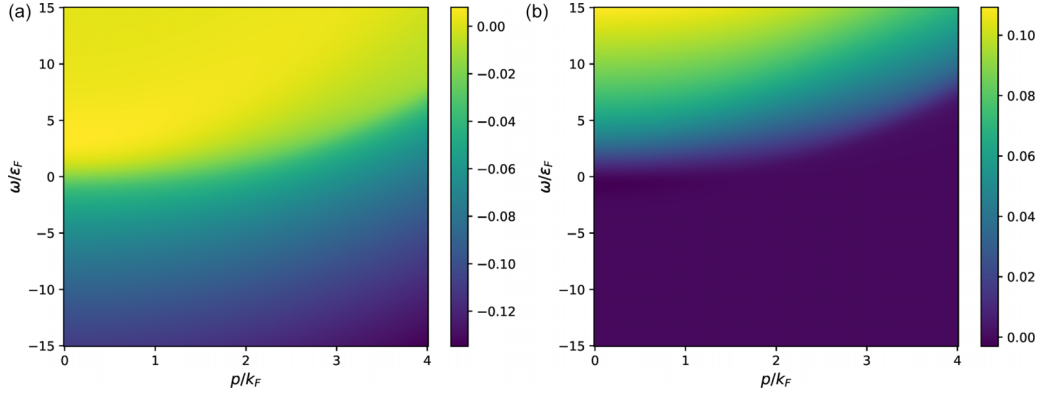
FIG. 11. (a) Real and (b) imaginary parts of the retarded boson self-energy $\Pi_\phi^R(\omega, \boldsymbol{p})$ for the balanced Fermi gas at unitarity and $T/T_F = 0.56$ ($\beta\mu = 0.13$).

computed numerically. Starting from Eq. (16), we define

$$\Sigma_\psi(\omega_n, \boldsymbol{p}) = \int_{\lambda_1, \lambda_2, \boldsymbol{q}} \rho_\phi(\lambda_1, \boldsymbol{q}) \rho_\psi(\lambda_2, \boldsymbol{p} - \boldsymbol{q}) I(\omega_n, \lambda_1, \lambda_2),$$

(C1)

with the analytic Matsubara sum over bosonic frequencies $\epsilon_m = 2m\pi T$,

$$I(\omega_n, \lambda_1, \lambda_2) = T \sum_{\epsilon_m} \frac{1}{i\epsilon_m - \lambda_1} \frac{1}{i(\epsilon_m - \omega_n) - \lambda_2}$$

$$= \frac{-n_B(\lambda_1) - n_F(\lambda_2)}{-i\omega_n + \lambda_1 - \lambda_2}. \quad \text{(C2)}$$

Performing the analytic continuation $i\omega_n \rightarrow \omega + i0^+$ and taking the imaginary part, we recover Eq. (20). Note that the pole in $n_B(\lambda_1)$ at $\lambda_1 = 0$ is exactly canceled by the zero transition of $\rho_\phi(\lambda_1)$.

For the numerical computation of the fermion self-energy, the high-frequency tails contribute significantly. Therefore, we adopt a semianalytic treatment, which is discussed in Appendix D and improves the determination of the real part via Kramers-Kronig substantially. An exemplary plot of the fully converged fermion self-energy $\Sigma_\psi^R(\omega, \boldsymbol{p})$ is shown in Fig. 12.

APPENDIX D: EXISTENCE OF THE SPECTRAL REPRESENTATION

While the propagator, or two-point function, of the fermionic atom field is that of a physical particle and hence has a spectral representation, such a representation may not hold for the composite bosonic dimer field. Moreover, even in the case of the existence of spectral representations for both fields, they may not be present in given approximations. Within the present spectral functional DSE approach, both the absence of a spectral representation and its failure in a given approximation are signaled by a lack of convergence of the iterative procedure underlying the solution of the DSE. This has been discussed in detail in [56] using the example of Yang-Mills theory. In turn, if such a convergent solution of the coupled system of DSEs for the spectral functions $\rho_{\psi/\phi}$ exists, this proves the existence of the spectral representation for both fields in the given approximation: By definition, the diagrammatic part carries the correct complex structure underlying the spectral representation, and the iterative solution of the system of spectral gap equations only converges if (12) with (13) provides the full propagator.

Here we demonstrate explicitly that the spectral representation of the propagators, evaluated at imaginary frequencies, agrees with the diagrammatic solution of the imaginary-time gap equation: In Figs. 13 and 14 we compare the full
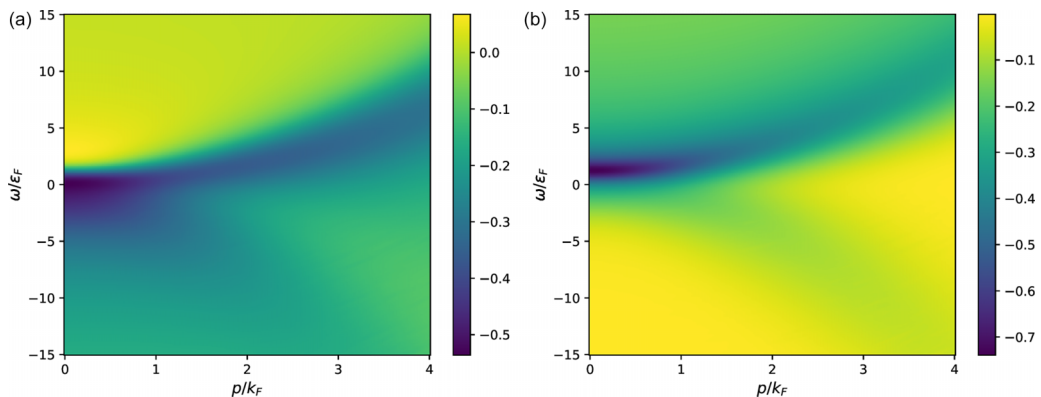

FIG. 12. (a) Real and (b) imaginary parts of the retarded fermion self-energy $\Sigma_\psi^R(\omega, \boldsymbol{p})$ for the balanced Fermi gas at unitarity and $T/T_F = 0.56$ ($\beta\mu = 0.13$).
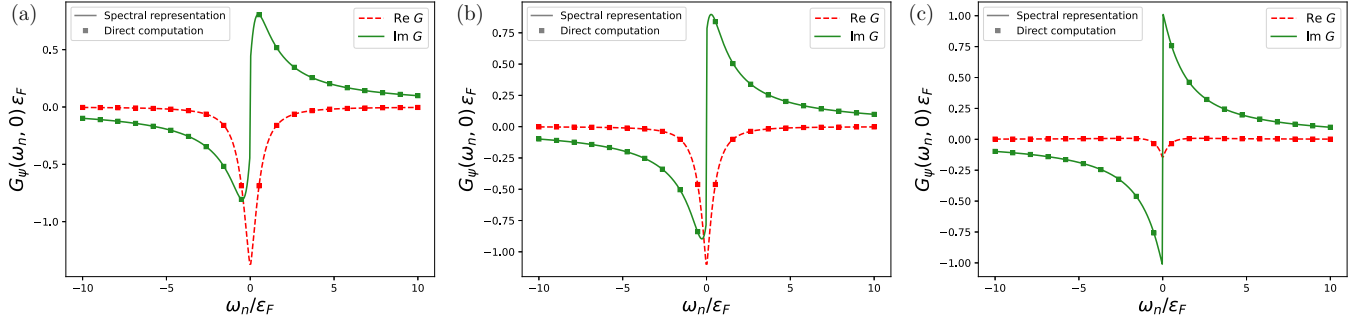
FIG. 13. Comparison of the full fermionic imaginary-time propagator $G_\psi(\omega_n, \mathbf{0})\varepsilon_F$ for $T/T_F = 0.56$ at different interaction strengths (a) $(k_F a)^{-1} = -0.5$, (b) $(k_F a)^{-1} = 0$, and (c) $(k_F a)^{-1} = 0.5$, obtained from the spectral representation (12) and directly from the gap equation (8) at imaginary frequencies. Respective results for the spectral function $\rho_\psi(\omega, \mathbf{p})\varepsilon_F$ at the same interaction strengths are shown in Fig. 3.

fermionic and bosonic imaginary-time propagators, respectively, obtained from the spectral representation in Eq. (12) (solid lines) with that obtained within a direct evaluation of the gap equation in Eq. (8) at imaginary frequencies (square data points). The propagators from these two procedures agree within the numerical errors and this agreement also extends to finite momenta (see Figs. 15 and 16).

APPENDIX E: NUMERICAL IMPLEMENTATION

The numerical iteration is done with a standard iteration procedure for integral equations. The first iteration step is done for the bosonic propagator and only involves the classical fermion propagators. The following one for the fermion propagator includes the results of the first step for the bosonic propagator and again uses the classical fermion propagator. All the remaining ones use the fully numerical results from the previous steps. The respective workflow can be summarized as follows.

(1) First iteration of the boson propagator. Start with the analytic expression for $\mathrm{Im}\Pi_\phi^R$ and calculate $\mathrm{Re}\Pi_\phi^R$ on a finite grid. To simplify the calculation, treat the divergent vacuum part analytically (discussed below). Choose a grid size large enough such that the numerical corrections are small. This can be quantified in dependence on the temperature.

(2) First iteration of the fermion propagator. Take the classical fermion spectral function (δ peak) and the semianalytic

boson spectral function from the first iteration and calculate $\mathrm{Im}\Sigma_\psi^R$ with (20) on a finite grid. From this, obtain $\mathrm{Re}\Sigma_\psi^R$ as described below.

(3) Further iterations of the fermion propagator. Take the numerical spectral functions for the fermion and boson and calculate the self-energy as in step 2.

(4) Further iterations of the boson propagator. Take numerical spectral functions for the fermions and calculate $\mathrm{Im}\Pi_\phi^R$ on a finite grid. Compute the difference from the non-self-consistent result and obtain the real part. Outside the grid, glue smoothly to the semianalytical non-self-consistent result.

For the numerical calculation of the two-dimensional functions, an adaptive method is used. The sampling points are chosen automatically based on the functional form. Fewer samples are taken in slowly varying regions and more samples are taken in faster varying regions. Additionally, the calculation of these sampling points can be parallelized over multiple cores. The resulting sampling points are then linearly interpolated. It is useful to simplify the interpolation by transforming the functions onto the quadratic dispersion relation. For the bosonic self-energy, this step can significantly improve the resolution of sharp edges in the function. For the fermionic self-energy, it can additionally help to ensure a large enough distance of the grid boundary to the main peak such that asymptotic behavior is guaranteed for all momenta.

The numerical integration of the three-dimensional self-energy loop integrals is performed mainly with an adaptive
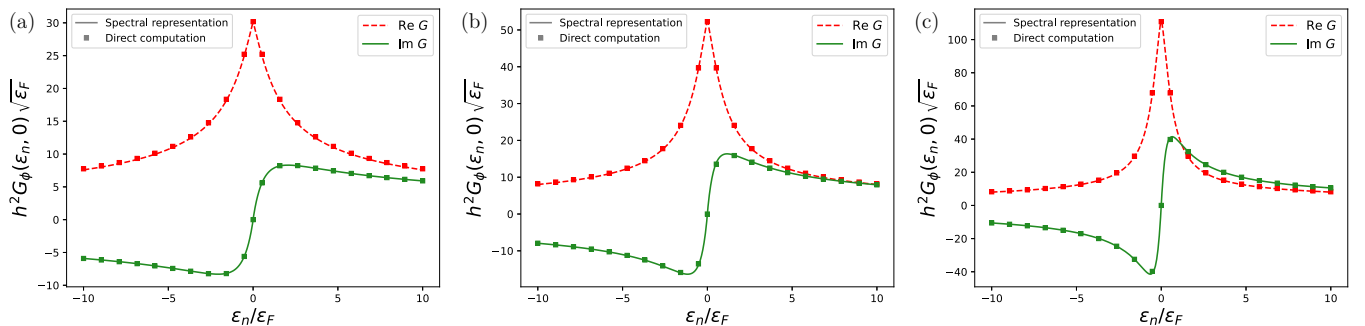

FIG. 14. Comparison of the full bosonic imaginary-time propagator $h^2 G_\phi(\varepsilon_n, \mathbf{0})\sqrt{\varepsilon_F}$ for $T/T_F = 0.56$ at different interaction strengths (a) $(k_F a)^{-1} = -0.5$, (b) $(k_F a)^{-1} = 0$, and (c) $(k_F a)^{-1} = 0.5$, obtained from the spectral representation (12) and directly from the gap equation (8) at imaginary frequencies. Respective results for the spectral function $h^2 \rho_\phi(\omega, \mathbf{p})\sqrt{\varepsilon_F}/8\pi$ at the same interaction strengths are shown in Fig. 4.
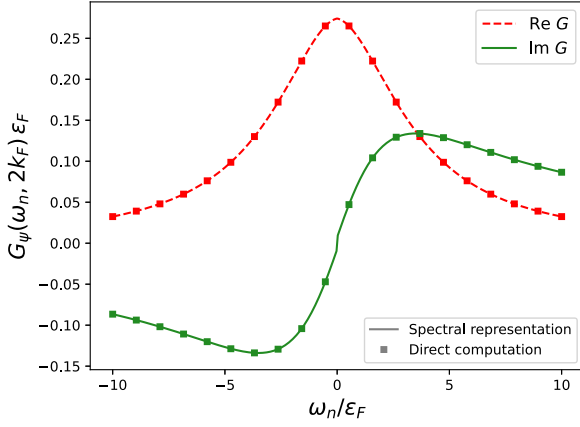
FIG. 15. Full fermionic imaginary-time propagator $G_\psi(\omega_n, 2k_F)\varepsilon_F$ for $T/T_F = 0.56$ at momentum $\|\boldsymbol{p}\| = 2k_F$ and unitarity, obtained from the spectral representation (12) and directly from the gap equation (8) at imaginary frequencies.

Monte Carlo method. This allows for maximal flexibility when dealing with highly peaked integrands in a multidimensional space and can be generalized easily towards further classes of diagrams. However, it comes with the downside of a long runtime in comparison to standard adaptive routines in low dimensions like here. For this specific case, a different adaptive integration routine using sparse grids is far more efficient. The one-dimensional principal value integral for the real part of the self-energy is computed efficiently using an adaptive quadrature integration.

For the representation of the numerical self-energy on the finite grid, an adaptive grid is chosen for the imaginary and real parts, separately. Typical boundaries in frequency are $\omega = [-200, 200]\varepsilon_F$ and in momentum $p = [0, 10]k_F$. Approximately 10.000–20.000 grid points are needed to obtain stable numerical results.
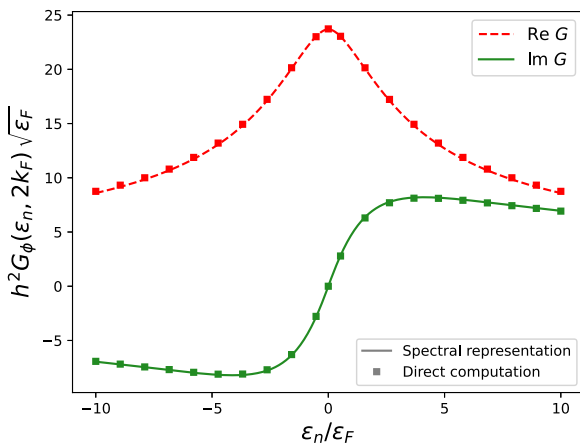

FIG. 16. Full bosonic imaginary-time propagator $h^2 G_\phi(\varepsilon_n, 2k_F)\sqrt{\varepsilon_F}$ for $T/T_F = 0.56$ at momentum $\|\boldsymbol{p}\| = 2k_F$ and unitarity, obtained from the spectral representation (12) and directly from the gap equation (8) at imaginary frequencies.

1. Boson spectral function

In this section we detail the numerical calculation and representation of the boson spectral function ρ_ϕ. Since the vacuum part of the bosonic self-energy is problematic, the numerical procedure requires suitable subtraction schemes and analytic treatment.

As seen above, the vacuum contribution to the boson self-energy is given by

$$\Pi_\phi^0(\epsilon_n, \boldsymbol{p}) = -\frac{h^2}{8\pi}\sqrt{-\frac{i\epsilon_n}{2} + \frac{\boldsymbol{p}^2}{4} - \mu}. \qquad (E1)$$

With (E1), the (retarded) imaginary part follows as

$$\operatorname{Im}\Pi_\phi^{R,0}(\omega, \boldsymbol{p}) = \frac{h^2}{8\pi}\sqrt{\frac{\omega}{2} - \frac{\boldsymbol{p}^2}{4} + \mu}. \qquad (E2)$$

In order to obtain the full real part $\operatorname{Re}\Pi_\phi^R$ of the self-energy via the Kramers-Kronig relation numerically, we can subtract Eq. (E2) from the total numerical imaginary part $\operatorname{Im}\Pi_\phi^R$ and find

$$\operatorname{Re}\Pi_\phi^R(\omega, \boldsymbol{p}) = \operatorname{Re}\Pi_\phi^{R,0}(\omega, \boldsymbol{p})$$
$$+ \frac{1}{\pi}\int_\lambda \frac{\operatorname{Im}\Pi_\phi^R(\lambda, \boldsymbol{p}) - \operatorname{Im}\Pi_\phi^{R,0}(\lambda, \boldsymbol{p})}{\lambda - \omega}, \quad (E3)$$

where the real part of the vacuum solution is

$$\operatorname{Re}\Pi_\phi^{R,0}(\omega, \boldsymbol{p}) = -\frac{h^2}{8\pi}\sqrt{-\frac{\omega}{2} + \frac{\boldsymbol{p}^2}{4} - \mu}. \qquad (E4)$$

With these formulas, we can obtain $\operatorname{Im}\Pi_\phi^R$ and $\operatorname{Re}\Pi_\phi^R$ on a finite grid numerically. However, the calculation of the real part requires also information about the high-frequency tails outside the numerical grid. In this case, the imaginary part outside the grid is approximated by the analytic formula of the non-self-consistent self-energy discussed in Appendix D,

$$\operatorname{Im}\Pi_\phi^R(\omega, \boldsymbol{p}) - \operatorname{Im}\Pi_\phi^{R,0}(\omega, \boldsymbol{p}) \approx \operatorname{Im}\Pi_\phi^{R,T}(\omega, \boldsymbol{p}) \qquad (E5)$$

for large ω. Thus, the bosonic spectral function outside the grid is approximated by the non-self-consistent (first iteration) spectral function $\rho_\phi^{(1)}$. A different subtraction scheme would be to subtract the whole non-self-consistent imaginary part straight away and only deal with differences from the first iteration. In principle, both methods are equivalent and work similarly. For practical reasons, we choose the latter subtraction scheme.

Another trick to improve the numerical calculation was already mentioned above. Since the boson self-energy follows a quadratic dispersion relation, it is practical to transform the functions into the dispersion relation before interpolation. This way, a better sampling and interpolation of the important regions can be achieved. Afterward, the interpolated function is shifted back to the correct dispersion relation.

Since the fermion spectral functions in the self-energy integrals are very peaked for lower temperatures and higher momenta, it might be useful to subtract a broadened classical spectral function, or the first iteration, from the further iterations in order to improve the integration for higher momenta. The contribution from the subtracted spectral function then has to be taken into account. Since the fermion spectral functions are represented on a finite numerical grid, the bare

δ peak contributions from outside the grid has to be taken into account too. This is similar to the peak-tail splits from [49].

2. Calculation of the real part via the Kramers-Kronig relation

It turns out that the calculation of the real part via the Kramers-Kronig relation is very sensitive to the high-frequency tails of the imaginary part. We accommodate for this fact with an extrapolation of the high-frequency tail, which allows us to estimate its contribution. For constant momentum p, the high-frequency asymptotics of the fermion self-energy is captured by the power law

$$\lim_{\omega \to \infty} \text{Im}\Sigma_{\psi}^{R}(\omega) = a\omega^{-1/2}, \qquad (E6)$$

where the constant a is determined by a fitting routine. From this fit we can calculate the missing contribution for the real part at a frequency ω via

$$\delta \, \text{Re}\Sigma_{\psi}^{R}(\omega) = \frac{2a}{\pi\sqrt{\Delta}} {}_2F_1\left(\frac{1}{2}, \frac{1}{2}; \frac{3}{2}; -\frac{\omega}{\Delta}\right), \qquad (E7)$$

where $\Delta = \omega_{\max} - \omega$, $\omega_{\max}$ is the highest frequency of the grid, and ${}_2F_1(a, b; c; z)$ is the hypergeometric function [104]. Using this high-frequency contribution from outside the grid improves the determination of the fermion real part significantly.

This asymptotic behavior can be shown by arguments similar to those in Ref. [85]. We consider the high-frequency behavior and rewrite the imaginary part of the fermion self-energy (20) as

$$\text{Im}\Sigma_{\psi}^{R}(\omega) \sim \int_{\lambda_1, \lambda_2, \boldsymbol{q}} \rho_\phi(\lambda_1)\rho_\psi(\lambda_2)\delta(\omega - \lambda_1 + \lambda_2)$$
$$\times [n_B(\lambda_1) + n_F(\lambda_2)]. \qquad (E8)$$

In the limit $\omega \to \infty$, the δ function contributes only if (a) λ_1 is large and λ_2 is small or (b) λ_2 is a large negative value and λ_1 is small. In case (b), however, the fermion spectral function ρ_ψ vanishes for low momenta and $\lambda_2 \to -\infty$. Thus, only case (a) contributes and we are left with

$$\text{Im}\Sigma_{\psi}^{R}(\omega) \sim \int_{\lambda_2, \boldsymbol{q}} \rho_\phi(\omega + \lambda_2)\rho_\psi(\lambda_2)n_F(\lambda_2), \qquad (E9)$$

where we have used $n_B(\lambda_1) \to 0$ for $\lambda_1 \to \infty$. As seen above, the high-frequency behavior of the boson spectral function is dominated by $\rho_\phi(\omega) \sim 1/\sqrt{\omega}$. Additionally, the integrand vanishes for large negative values of λ_2, since $\rho_\psi(\lambda_2)$ vanishes, and for large positive values of λ_2, since $n_F(\lambda_2)$ vanishes. Thus, the range of λ_2 is limited and we can write

$$\text{Im}\Sigma_{\psi}^{R}(\omega) \sim \int_{\lambda_2, \boldsymbol{q}} \rho_\psi(\lambda_2)n_F(\lambda_2)/\sqrt{\omega} \sim 1/\sqrt{\omega}, \qquad (E10)$$

where we used that $\int_{\lambda_2, \boldsymbol{q}} \rho_\psi(\lambda_2)n_F(\lambda_2) = n$ is finite in the last step. With the same argument we can show that $\text{Im}\Sigma_{\psi}^{R}(\omega)$ is mostly suppressed for large negative frequencies.

3. Iterative procedure

Using (20), (19), and the Kramers-Kronig relation, the retarded self-energies can be computed in every iteration step and fed back into the next, after extraction of the spectral function via Eq. (13). The iterative procedure is initialized with the classical fermion spectral function

$$\rho_{\psi}^{(0)}(\omega, \boldsymbol{p}) = \delta(\omega - \boldsymbol{p}^2 + \mu). \qquad (E11)$$

This initial guess is inserted into the spectral form of $\Pi_\phi(P)$ to obtain the first iteration of the boson spectral function $\rho_\phi^{(1)}$. Then $\rho_\phi^{(1)}$ together with $\rho_\psi^{(0)}$ is inserted into the spectral integral of $\Sigma_\psi(P)$ to obtain the first iteration of the fermion spectral function $\rho_\psi^{(1)}$. Now $\rho_\psi^{(1)}$ can be used to obtain the next iteration for the boson spectral function $\rho_\phi^{(2)}$ and so on. In general, $\rho_\psi^{(i)}$ is used to obtain $\rho_\phi^{(i+1)}$, and $\rho_\phi^{(i+1)}$ and $\rho_\psi^{(i)}$ are used to obtain $\rho_\psi^{(i+1)}$. This iteration is repeated until convergence is reached. We observe that around 5–20 iterations are needed to obtain a converged result with

$$\int_{\lambda} \|\rho^{(i)}(\lambda, \boldsymbol{p}) - \rho^{(i-1)}(\lambda, \boldsymbol{p})\| \lesssim 0.005 \,\forall\, \boldsymbol{p}. \qquad (E12)$$

As mentioned in the main text, the convergence is worse closer to the critical temperature and the spectral functions may oscillate between intermediate solutions. One can improve the convergence by iterating twice over the fermions or updating the spectral functions only partially.

[1] I. Bloch, J. Dalibard, and W. Zwerger, Many-body physics with ultracold gases, Rev. Mod. Phys. **80**, 885 (2008).

[2] S. Giorgini, L. P. Pitaevskii, and S. Stringari, Theory of ultracold atomic Fermi gases, Rev. Mod. Phys. **80**, 1215 (2008).

[3] W. Zwerger, *in Quantum Matter at Ultralow Temperatures*, Proceedings of the International School of Physics "Enrico Fermi," Course CXCI, Varenna, 2016, edited by M. Inguscio, W. Ketterle, S. Stringari, and G. Roati (IOS, Amsterdam, 2016), pp. 63–142.

[4] M. Greiner, C. A. Regal, and D. S. Jin, Emergence of a molecular Bose–Einstein condensate from a Fermi gas, Nature (London) **426**, 537 (2003).

[5] C. Chin, M. Bartenstein, A. Altmeyer, S. Riedl, S. Jochim, J. H. Denschlag, and R. Grimm, Observation of the pairing gap in a strongly interacting Fermi gas, Science **305**, 1128 (2004).

[6] A. Perali, P. Pieri, L. Pisani, and G. C. Strinati, BCS-BEC crossover at finite temperature for superfluid trapped Fermi atoms, Phys. Rev. Lett. **92**, 220404 (2004).

[7] B. Mukherjee, P. B. Patel, Z. Yan, R. J. Fletcher, J. Struck, and M. W. Zwierlein, Spectral response and contact of the unitary Fermi gas, Phys. Rev. Lett. **122**, 203402 (2019).

[8] G. C. Strinati, P. Pieri, G. Röpke, P. Schuck, and M. Urban, The BCS–BEC crossover: From ultra-cold Fermi gases to nuclear systems, Phys. Rep. **738**, 1 (2018).

[9] A. Schirotzek, C.-H. Wu, A. Sommer, and M. W. Zwierlein, Observation of Fermi polarons in a tunable Fermi liquid of ultracold atoms, Phys. Rev. Lett. **102**, 230402 (2009).

[10] S. Nascimbène, N. Navon, K. J. Jiang, L. Tarruell, M. Teichmann, J. McKeever, F. Chevy, and C. Salomon, Collective oscillations of an imbalanced Fermi gas: Axial

compression modes and polaron effective mass, Phys. Rev. Lett. **103**, 170402 (2009).

[11] P. Massignan, M. Zaccanti, and G. M. Bruun, Polarons, dressed molecules and itinerant ferromagnetism in ultracold Fermi gases, Rep. Prog. Phys. **77**, 034401 (2014).

[12] G. Ness, C. Shkedrov, Y. Florshaim, O. K. Diessel, J. von Milczewski, R. Schmidt, and Y. Sagi, Observation of a smooth polaron-molecule transition in a degenerate Fermi gas, Phys. Rev. X **10**, 041019 (2020).

[13] F. Scazza, M. Zaccanti, P. Massignan, M. M. Parish, and J. Levinsen, Repulsive Fermi and Bose polarons in quantum gases, Atoms **10**, 55 (2022).

[14] M. W. Zwierlein, J. R. Abo-Shaeer, A. Schirotzek, C. H. Schunck, and W. Ketterle, Vortices and superfluidity in a strongly interacting Fermi gas, Nature (London) **435**, 1047 (2005).

[15] M. W. Zwierlein, A. Schirotzek, C. H. Schunck, and W. Ketterle, Fermionic superfluidity with imbalanced spin populations, Science **311**, 492 (2006).

[16] M. J. H. Ku, A. T. Sommer, W. C. Lawrence, and M. W. Zwierlein, Revealing the superfluid lambda transition in the universal thermodynamics of a unitary Fermi gas, Science **335**, 563 (2012).

[17] E. Burovski, N. Prokof'ev, B. Svistunov, and M. Troyer, Critical temperature and thermodynamics of attractive fermions at unitarity, Phys. Rev. Lett. **96**, 160402 (2006).

[18] P. Magierski, G. Wlazlowski, A. Bulgac, and J. E. Drut, The finite temperature pairing gap of a unitary Fermi gas by quantum Monte Carlo, Phys. Rev. Lett. **103**, 210403 (2009).

[19] R. Haussmann, W. Rantner, S. Cerrito, and W. Zwerger, Thermodynamics of the BCS-BEC crossover, Phys. Rev. A **75**, 023610 (2007).

[20] H. Hu, X.-J. Liu, and P. D. Drummond, Comparative study of strong-coupling theories of a trapped Fermi gas at unitarity, Phys. Rev. A **77**, 061605(R) (2008).

[21] C.-C. Chien, H. Guo, Y. He, and K. Levin, Comparative study of BCS-BEC crossover theories above T_c: The nature of the pseudogap in ultracold atomic Fermi gases, Phys. Rev. A **81**, 023622 (2010).

[22] R. Hanai and Y. Ohashi, Self-consistent T-matrix approach to an interacting ultracold Fermi Gas with mass imbalance, J. Low Temp. Phys. **175**, 272 (2014).

[23] R. B. Diener, R. Sensarma, and M. Randeria, Quantum fluctuations in the superfluid state of the BCS-BEC crossover, Phys. Rev. A **77**, 023626 (2008).

[24] S. Diehl and C. Wetterich, Universality in phase transitions for ultracold fermionic atoms, Phys. Rev. A **73**, 033615 (2006).

[25] I. Boettcher, S. Diehl, J. M. Pawlowski, and C. Wetterich, Tan contact and universal high momentum behavior of the fermion propagator in the BCS-BEC crossover, Phys. Rev. A **87**, 023606 (2013).

[26] S. Diehl, H. Gies, J. M. Pawlowski, and C. Wetterich, Flow equations for the BCS-BEC crossover, Phys. Rev. A **76**, 021602(R) (2007).

[27] S. Diehl, H. Gies, J. M. Pawlowski, and C. Wetterich, Renormalization flow and universality for ultracold fermionic atoms, Phys. Rev. A **76**, 053627 (2007).

[28] S. Diehl, S. Floerchinger, H. Gies, J. M. Pawlowski, and C. Wetterich, Functional renormalization group approach to the BCS-BEC crossover, Ann. Phys. (Berlin) **522**, 615 (2010).

[29] E. Taylor and M. Randeria, Viscosity of strongly interacting quantum fluids: Spectral functions and sum rules, Phys. Rev. A **81**, 053610 (2010).

[30] T. Enss, R. Haussmann, and W. Zwerger, Viscosity and scale invariance in the unitary Fermi gas, Ann. Phys. (NY) **326**, 770 (2011).

[31] B. Frank, W. Zwerger, and T. Enss, Quantum critical thermal transport in the unitary Fermi gas, Phys. Rev. Res. **2**, 023301 (2020).

[32] M. Greiner, C. A. Regal, and D. S. Jin, Probing the excitation spectrum of a Fermi gas in the BCS-BEC crossover regime, Phys. Rev. Lett. **94**, 070403 (2005).

[33] F. Palestini, A. Perali, P. Pieri, and G. C. Strinati, Dispersions, weights, and widths of the single-particle spectral function in the normal phase of a Fermi gas, Phys. Rev. B **85**, 024517 (2012).

[34] H. Biss, L. Sobirey, N. Luick, M. Bohlen, J. J. Kinnunen, G. M. Bruun, T. Lompe, and H. Moritz, Excitation spectrum and superfluid gap of an ultracold Fermi gas, Phys. Rev. Lett. **128**, 100401 (2022).

[35] M. Jarrell and J. E. Gubernatis, Bayesian inference and the analytic continuation of imaginary-time quantum Monte Carlo data, Phys. Rep. **269**, 133 (1996).

[36] A. K. Cyrol, J. M. Pawlowski, A. Rothkopf, and N. Wink, Reconstructing the gluon, SciPost Phys. **5**, 065 (2018).

[37] J. Horak, J. M. Pawlowski, J. Rodríguez-Quintero, J. Turnwald, J. M. Urban, N. Wink, and S. Zafeiropoulos, Reconstructing QCD spectral functions with Gaussian processes, Phys. Rev. D **105**, 036014 (2022).

[38] R. Haussmann, M. Punk, and W. Zwerger, Spectral functions and rf response of ultracold fermionic atoms, Phys. Rev. A **80**, 063612 (2009).

[39] R. Schmidt and T. Enss, Excitation spectra and rf response near the polaron-to-molecule transition from the functional renormalization group, Phys. Rev. A **83**, 063620 (2011).

[40] J. Schmalian, M. Langer, S. Grabowski, and K. H. Bennemann, Self-consistent summation of many-particle diagrams on the real frequency axis and its application to the FLEX approximation, Comput. Phys. Commun. **93**, 141 (1996).

[41] B. Kyung, E. G. Klepfish, and P. E. Kornilovitch, Density-induced breaking of pairs in the attractive Hubbard model, Phys. Rev. Lett. **80**, 3109 (1998).

[42] D. Rohe and W. Metzner, Pair-fluctuation-induced pseudogap in the normal phase of the two-dimensional attractive Hubbard model at weak coupling, Phys. Rev. B **63**, 224509 (2001).

[43] C. P. Moca and E. Macocian, Transport properties calculation in the superconducting state for a quasi-two-dimensional system, Physica C **356**, 268 (2001).

[44] A. Perali, P. Pieri, G. C. Strinati, and C. Castellani, Pseudogap and spectral function from superconducting fluctuations to the bosonic limit, Phys. Rev. B **66**, 024510 (2002).

[45] P. Pieri, L. Pisani, and G. C. Strinati, Pairing fluctuation effects on the single-particle spectra for the superconducting state, Phys. Rev. Lett. **92**, 110401 (2004).

[46] P. Pieri, L. Pisani, and G. C. Strinati, BCS-BEC crossover at finite temperature in the broken-symmetry phase, Phys. Rev. B **70**, 094508 (2004).

[47] E. Fratini and P. Pieri, Single-particle spectral functions in the normal phase of a strongly attractive Bose-Fermi mixture, Phys. Rev. A **88**, 013627 (2013).

[48] H. Hu and X.-J. Liu, Fermi polarons at finite temperature: Spectral function and rf spectroscopy, Phys. Rev. A **105**, 043303 (2022).

[49] J. Horak, J. M. Pawlowski, and N. Wink, Spectral functions in the ϕ^4-theory from the spectral Dyson-Schwinger equations, Phys. Rev. D **102**, 125016 (2020).

[50] J. Fehre, D. F. Litim, J. M. Pawlowski, and M. Reichert, Lorentzian quantum gravity and the graviton spectral function, Phys. Rev. Lett. **130**, 081501 (2023).

[51] J. Braun *et al.*, Renormalised spectral flows, SciPost Phys. Core **6**, 061 (2023).

[52] J. Berges, Introduction to nonequilibrium quantum field theory, AIP Conf. Proc. **739**, 3 (2004).

[53] J. Horak, F. Ihssen, J. M. Pawlowski, J. Wessely, and N. Wink, Scalar spectral functions from the spectral fRG, arXiv:2303.16719.

[54] G. Eichmann, A. Gómez, J. Horak, J. M. Pawlowski, J. Wessely, and N. Wink, Bound states from the spectral Bethe-Salpeter equation, Phys. Rev. D **109**, 096024 (2024).

[55] J. Horak, J. M. Pawlowski, and N. Wink, On the quark spectral function in QCD, SciPost Phys. **15**, 149 (2023).

[56] J. Horak, J. M. Pawlowski, and N. Wink, On the complex structure of Yang-Mills theory, arXiv:2202.09333.

[57] J. Horak, J. Papavassiliou, J. M. Pawlowski, and N. Wink, Ghost spectral function from the spectral Dyson-Schwinger equation, Phys. Rev. D **104**, 074017 (2021).

[58] J. Horak, Realtime properties of QCD, Ph.D. thesis, Universität Heidelberg, 2023.

[59] C. Chin, R. Grimm, P. Julienne, and E. Tiesinga, Feshbach resonances in ultracold gases, Rev. Mod. Phys. **82**, 1225 (2010).

[60] R. Rossi, T. Ohgoe, E. Kozik, N. Prokof'ev, B. Svistunov, K. Van Houcke, and F. Werner, Contact and momentum distribution of the unitary Fermi gas, Phys. Rev. Lett. **121**, 130406 (2018).

[61] H. Gies and C. Wetterich, Renormalization flow of bound states, Phys. Rev. D **65**, 065001 (2002).

[62] J. M. Pawlowski, Aspects of the functional renormalisation group, Ann. Phys. (NY) **322**, 2831 (2007).

[63] S. Floerchinger and C. Wetterich, Exact flow equation for composite operators, Phys. Lett. B **680**, 371 (2009).

[64] W.-j. Fu, J. M. Pawlowski, and F. Rennecke, QCD phase structure at finite temperature and density, Phys. Rev. D **101**, 054032 (2020).

[65] S. Floerchinger, M. Scherer, S. Diehl, and C. Wetterich, Particle-hole fluctuations in the BCS-BEC Crossover, Phys. Rev. B **78**, 174528 (2008).

[66] S. Floerchinger, M. M. Scherer, and C. Wetterich, Modified Fermi-sphere, pairing gap and critical temperature for the BCS-BEC crossover, Phys. Rev. A **81**, 063619 (2010).

[67] P. Nozieres and S. Schmitt-Rink, Bose condensation in an attractive fermion gas: From weak to strong coupling superconductivity, J. Low Temp. Phys. **59**, 195 (1985).

[68] C. A. R. Sá de Melo, M. Randeria, and J. R. Engelbrecht, Crossover from BCS to Bose superconductivity: Transition temperature and time-dependent Ginzburg-Landau theory, Phys. Rev. Lett. **71**, 3202 (1993).

[69] Q. Chen, J. Stajic, S. Tan, and K. Levin, BCS–BEC crossover: From high temperature superconductors to ultracold superfluids, Phys. Rep. **412**, 1 (2005).

[70] E. S. Swanson, A primer on functional methods and the Schwinger-Dyson equations, AIP Conf. Proc. **1296**, 75 (2010).

[71] P. Kopietz, L. Bartosch, and F. Schütz, *Introduction to the Functional Renormalization Group*, Lecture Notes in Physics Vol. 798 (Springer, Berlin, 2010).

[72] W. Metzner, M. Salmhofer, C. Honerkamp, V. Meden, and K. Schonhammer, Functional renormalization group approach to correlated fermion systems, Rev. Mod. Phys. **84**, 299 (2012).

[73] M. M. Scherer, S. Floerchinger, and H. Gies, Functional renormalization for the Bardeen–Cooper–Schrieffer to Bose–Einstein condensation crossover, Phil. Trans. R. Soc. A **369**, 2779 (2011).

[74] I. Boettcher, J. M. Pawlowski, and S. Diehl, Ultracold atoms and the functional renormalization group, Nucl. Phys. B **228**, 63 (2012).

[75] N. Dupuis, L. Canet, A. Eichhorn, W. Metzner, J. M. Pawlowski, M. Tissier, and N. Wschebor, The nonperturbative functional renormalization group and its applications, Phys. Rep. **910**, 1 (2021).

[76] M. Pini, P. Pieri, and G. C. Strinati, Fermi gas throughout the BCS-BEC crossover: Comparative study of t-matrix approaches with various degrees of self-consistency, Phys. Rev. B **99**, 094502 (2019).

[77] A. A. Abrikosov, L. P. Gorkov, and I. E. Dzyaloshinski, *Methods of Quantum Field Theory in Statistical Physics* (Dover, New York, 1975).

[78] A. L. Fetter and J. D. Walecka, *Quantum Theory of Many-Particle Systems* (McGraw-Hill, New York, 1971).

[79] M. D. Reichl and E. J. Mueller, Quasiparticle dispersions and lifetimes in the normal state of the BCS-BEC crossover, Phys. Rev. A **91**, 043627 (2015).

[80] D. J. Thouless, Perturbation theory in statistical mechanics and the theory of superconductivity, Ann. Phys. (NY) **10**, 553 (1960).

[81] C. H. Johansen, B. Frank, and J. Lang, Spectral functions of the strongly interacting three-dimensional Fermi gas, Phys. Rev. A **109**, 023324 (2024).

[82] T. Enss, Particle and pair spectra for strongly correlated Fermi gases: A real-frequency solver, Phys. Rev. A **109**, 023325 (2024).

[83] M. Punk and W. Zwerger, Theory of rf-spectroscopy of strongly interacting fermions, Phys. Rev. Lett. **99**, 170404 (2007).

[84] J. Stewart, J. Gaebler, and D. Jin, Using photoemission spectroscopy to probe a strongly interacting Fermi gas, Nature (London) **454**, 744 (2008).

[85] W. Schneider, V. B. Shenoy, and M. Randeria, Theory of radio frequency spectroscopy of polarized Fermi gases, arXiv:0903.3006.

[86] S. Tsuchiya, R. Watanabe, and Y. Ohashi, Photoemission spectrum and effect of inhomogeneous pairing fluctuations in the BCS-BEC crossover regime of an ultracold Fermi gas, Phys. Rev. A **82**, 033629 (2010).

[87] M. Veillette, E. G. Moon, A. Lamacraft, L. Radzihovsky, S. Sachdev, and D. E. Sheehy, Radio-frequency spectroscopy

of a strongly imbalanced Feshbach-resonant Fermi gas, Phys. Rev. A **78**, 033614 (2008).

[88] H. Tajima and S. Uchino, Thermal crossover, transition, and coexistence in Fermi polaronic spectroscopies, Phys. Rev. A **99**, 063606 (2019).

[89] D. Kagamihara, D. Inotani, and Y. Ohashi, Shear viscosity and strong-coupling corrections in the BCS–BEC crossover regime of an ultracold Fermi gas, J. Phys. Soc. Jpn. **88**, 114001 (2019).

[90] L. Pisani, M. Pini, P. Pieri, and G. C. Strinati, Peaks and widths of radio-frequency spectra: An analysis of the phase diagram of ultra-cold Fermi gases, Results Phys. **57**, 107358 (2024).

[91] H. Hu and X.-J. Liu, Spectral function of Fermi polarons at finite temperature from a self-consistent many-body T-matrix approach in real frequency, arXiv:2311.11554.

[92] X. Li *et al.*, Observation and quantification of the pseudogap in unitary Fermi gases, Nature (London) **626**, 288 (2024).

[93] R. Schmidt, T. Enss, V. Pietilä, and E. Demler, Fermi polarons in two dimensions, Phys. Rev. A **85**, 021602(R) (2012).

[94] J. E. Drut, T. A. Lahde, and T. Ten, Momentum distribution and contact of the unitary Fermi gas, Phys. Rev. Lett. **106**, 205302 (2011).

[95] B. Frank, Thermodynamics and transport in Fermi gases near unitarity, Ph.D. thesis, TU München, 2018.

[96] J. E. Drut, T. A. Lahde, G. Wlazlowski, and P. Magierski, The equation of state of the unitary Fermi gas: An update on lattice calculations, Phys. Rev. A **85**, 051601(R) (2012).

[97] J. E. Drut, Improved lattice operators for nonrelativistic fermions, Phys. Rev. A **86**, 013604 (2012).

[98] L. Rammelmüller, A. C. Loheac, J. E. Drut, and J. Braun, Finite-temperature equation of state of polarized fermions at unitarity, Phys. Rev. Lett. **121**, 173001 (2018).

[99] S. Jensen, C. N. Gilbreth, and Y. Alhassid, Contact in the unitary Fermi gas across the superfluid phase transition, Phys. Rev. Lett. **125**, 043402 (2020).

[100] B. M. Faigle-Cedzich, J. M. Pawlowski, and C. Wetterich, Towards quantitative precision in ultracold atoms with functional renormalisation, arXiv:2307.14787.

[101] S. Tan, Large momentum part of a strongly correlated Fermi gas, Ann. Phys. (NY) **323**, 2971 (2008).

[102] E. Braaten and L. Platter, Exact relations for a strongly interacting Fermi gas from the operator product expansion, Phys. Rev. Lett. **100**, 205301 (2008).

[103] M. Bauer (unpublished).

[104] *Handbook of Mathematical Functions with Formulas, Graphs, and Mathematical Tables*, Natl. Bur. Stand. (U.S.) Appl. Math. Ser. 55, edited by M. Abramowitz and I. A. Stegun (U.S. GPO, Washington, DC, 1972).

[105] J. R. Engelbrecht, M. Randeria, and C. A. R. Sá de Melo, BCS to Bose crossover: Broken-symmetry state, Phys. Rev. B **55**, 15153 (1997).

[106] J. von Milczewski and R. Schmidt, Momentum-dependent quasiparticle properties of the Fermi polaron from the functional renormalization group, arXiv:2312.05318.

[107] J. von Milczewski, F. Rose, and R. Schmidt, Functional-renormalization-group approach to strongly coupled Bose-Fermi mixtures in two dimensions, Phys. Rev. A **105**, 013317 (2022).

[108] Y. Guo, H. Tajima, T. Hatsuda, and H. Liang, BCS-BCS crossover between atomic and molecular superfluids in a Bose-Fermi mixture, Phys. Rev. A **108**, 023304 (2023).

[109] O. K. Diessel, J. von Milczewski, A. Christianen, and R. Schmidt, Probing molecular spectral functions and unconventional pairing using Raman spectroscopy, arXiv:2209.11758.

[110] L. M. Schonenberg, P. C. Verpoort, and G. J. Conduit, Effective-range dependence of two-dimensional Fermi gases, Phys. Rev. A **96**, 023619 (2017).

[111] M. Punk, Many-particle physics with ultracold gases, Ph.D. thesis, TU München, 2010.